Monthly Notices of the ROYAL ASTRONOMICAL SOCIETY

MNRAS **527,** 7203–7216 (2024) https://doi.org/10.1093/mnras/stad3066
Advance Access publication 2023 October 9

Sweeping secular resonances and giant planet inclinations in transition discs

J. J. Zanazzi [1]★† and E. Chiang[1,2]

[1]*Astronomy Department, Theoretical Astrophysics Center, and Center for Integrative Planetary Science, University of California Berkeley, Berkeley, CA 94720, USA*
[2]*Department of Earth and Planetary Science, University of California, Berkeley, CA 94720, USA*

Accepted 2023 October 3. Received 2023 September 27; in original form 2023 July 20

ABSTRACT

The orbits of some warm Jupiters are highly inclined (20°–50°) to those of their exterior companions. Comparable misalignments are inferred between the outer and inner portions of some transition discs. These large inclinations may originate from planet–planet and planet–disc secular resonances that sweep across interplanetary space as parent discs disperse. The maximum factor by which a seed mutual inclination can be amplified is of the order of the square root of the angular momentum ratio of the resonant pair. We identify those giant planet systems (e.g. Kepler-448 and Kepler-693) that may have crossed a secular resonance, and estimate the required planet masses and semimajor axes in transition discs needed to warp their innermost portions (e.g. in CQ Tau). Passage through an inclination secular resonance could also explain the hypothesized large mutual inclinations in apsidally-orthogonal warm Jupiter systems (e.g. HD 147018).

Key words: planets and satellites: dynamical evolution and stability – planets and satellites: formation – planet–disc interactions – protoplanetary discs.

1 INTRODUCTION

Most planetary systems are flat (e.g. Winn & Fabrycky 2015; Zhu & Dong 2021), but some are not. In addition to large stellar obliquities measured for single planets using the Rossiter–McLaughlin effect (e.g. Albrecht, Dawson & Winn 2022; Dong & Foreman-Mackey 2023; Siegel, Winn & Albrecht 2023), large mutual inclinations between planets have been suspected or confirmed. Dawson & Chiang (2014) proposed that certain warm Jupiters are inclined by $i_{\rm mut} \approx 40^\circ$ relative to exterior super-Jupiter companions, based on their relative apsidal orientations. Transit duration variations imply substantial misalignments in the warm Jupiter systems Kepler-448 ($i_{\rm mut} = 20^{+17}_{-12}{}^\circ$, Masuda 2017), Kepler-693 ($i_{\rm mut} = 53^{+7}_{-9}{}^\circ$, Masuda 2017), Kepler-108 ($i_{\rm mut} = 24^{+11}_{-8}{}^\circ$, Mills & Fabrycky 2017), and WASP-148 ($i_{\rm mut} = 21^{+5}_{-5}{}^\circ$, Almenara et al. 2022). The inclination between a cold Jupiter and inner super-Earth in π Men is astrometrically constrained to lie between $49^\circ < i_{\rm mut} < 131^\circ$ (Xuan & Wyatt 2020).

Some protoplanetary discs also exhibit large misalignments/warps. More than a dozen transitional discs (defined as having large cavities) are observed in scattered light to be shadowed by circumstellar material closer to their host stars (Benisty et al. 2022). Azimuthally extended shadows are cast by close-in discs inclined by $\sim 10^\circ$ relative to their outer discs (e.g. Stolker et al. 2016; Debes et al. 2017; Stolker et al. 2017; Muro-Arena et al. 2020), while narrow, diametrically opposed shadows are cast by the nodes of more highly inclined inner discs ($\sim 30^\circ$–90°; e.g. Marino, Perez & Casassus 2015; Benisty et al. 2017; Long et al. 2017; Casassus et al. 2018; Pinilla et al. 2018; Uyama et al. 2020; Ginski et al. 2021). Supporting evidence for misaligned discs comes from interferometric imaging (e.g. Kluska et al. 2020; GRAVITY Collaboration et al. 2021; Bohn et al. 2022) and CO kinematics (e.g. Casassus et al. 2015; Loomis et al. 2017; Mayama et al. 2018; Pérez et al. 2018; Bi et al. 2020; Kraus et al. 2020).

One mechanism for exciting inclinations is secular resonance. When two bodies precess nodally at the same rate, angular momentum can be efficiently transferred between them, lifting one orbit while lowering the other and amplifying $i_{\rm mut}$ in the net. Analogously, when apsidal precession rates match, eccentricities can change dramatically. Two planets can be driven through a secular resonance by their parent protoplanetary disc; as disc material depletes, planetary precession frequencies change, and can momentarily match. Secular resonance crossings driven by the depletion of the solar nebula may have excited the inclinations and eccentricities of the terrestrial planets, asteroids, and Kuiper belt objects (e.g. Ward, Colombo & Franklin 1976; Heppenheimer 1980; Ward 1981; Nagasawa & Ida 2000; Nagasawa, Tanaka & Ida 2000; Nagasawa, Ida & Tanaka 2001, 2002; Hahn 2003; Zheng, Lin & Kouwenhoven 2017).[1] Extrasolar versions of this scenario have also been invoked to explain warm Jupiter eccentricities (e.g. Nagasawa, Lin & Ida 2003; Petrovich,

★ E-mail: jzanazzi@berkeley.edu
† 51 Pegasi b fellow.

[1]Of course, direct gravitational scatterings (close encounters) can also play a role; see, e.g. Nesvorný (2018) and Brož et al. (2021).

Wu & Ali-Dib 2019; Teyssandier & Lai 2019) and spin-orbit misalignments of hot Jupiters (e.g. Lubow & Martin 2016; Martin et al. 2016; Spalding & Batygin 2017; Vick, Su & Lai 2023) and sub-Neptunes (Petrovich et al. 2020; Epstein-Martin, Becker & Batygin 2022). Petrovich et al. (2020) showed how a secular resonance between a gas giant and an interior sub-Neptune, both embedded in a decaying disc, could lift the sub-Neptune onto a polar orbit ($i_{\rm mut} \approx 90^\circ$).

We extend the works of Petrovich et al. (2020) and others by studying how the mutual inclinations of giant planets embedded in decaying transitional discs can be amplified by secular resonance passage. Our motivation includes misaligned giant planet systems like Kepler-448 and Kepler-693 (Masuda 2017), and the proposed class of mutually inclined, apsidally orthogonal warm Jupiters (Dawson & Chiang 2014). We also investigate how an inner disc can be tilted out of the plane of an outer disc by the action of an intermediary, gap-opening planet. Here, we build upon the disc-tilting calculations of Owen & Lai (2017) to study the parameter space occupied by transition discs shadowed by low-mass inner discs (Francis & van der Marel 2020; van der Marel et al. 2021). Section 2 lays out the basic theory for how a secular resonance crossing can excite the inclination and eccentricity of an inner warm Jupiter (Section 2.1), and the inclination of an inner disc (Section 2.2). Section 3 revisits the Dawson & Chiang (2014) hypothesis and updates the observed distribution of apsidal angles to see what might be inferred about mutual inclinations (Section 3.1), and then examines how introducing the stellar spin and mass quadrupole affects our general results (Section 3.2). Section 4 summarizes and connects further with the observations.

2 INCLINATION AND ECCENTRICITY EXCITATION FROM OUTER DISC MASS-LOSS

Consider a planet inside the cavity of a disc. The planet's longitude of pericentre ϖ and longitude of ascending node Ω precess at rates proportional to the disc's mass. As the disc's mass decreases, the magnitudes of the precession frequencies $|\dot{\varpi}|$ and $|\dot{\Omega}|$ decrease as well. If multiple bodies reside inside the cavity – a pair of planets, or a planet and an inner disc – their precession frequencies can be tuned down such that their respective apsidal or nodal longitudes align, or anti-align, for extended periods of time. As the bodies pass through such symmetric orbital configurations, angular momentum is transferred efficiently between them, with potentially large changes in eccentricity and inclination.

2.1 Two planets in a transition disc

We consider two planets surrounded by an outer disc. The disc's mass is prescribed to decrease with time. We compute the dynamical evolution in two ways, first using the Laplace–Lagrange secular equations (Section 2.1.1), and then with an N-body simulation (Sections 2.1.2–2.1.3).

2.1.1 Laplace–Lagrange theory

Planet eccentricities e, pericentre longitudes ϖ, inclinations i, and nodal longitudes Ω evolve according to

$$\frac{{\rm d}e_1}{{\rm d}t} = e_2 g_{12} \sin \Delta\varpi \tag{1}$$

$$\frac{{\rm d}e_2}{{\rm d}t} = -e_1 g_{21} \sin \Delta\varpi \tag{2}$$

$$\frac{{\rm d}\varpi_1}{{\rm d}t} = (f_{12} + f_{1{\rm d}}) - g_{12}\frac{e_2}{e_1}\cos \Delta\varpi \tag{3}$$

$$\frac{{\rm d}\varpi_2}{{\rm d}t} = (f_{21} + f_{2{\rm d}}) - g_{21}\frac{e_1}{e_2}\cos \Delta\varpi \tag{4}$$

$$\frac{{\rm d}s_1}{{\rm d}t} = -f_{12} s_2 \sin \Delta\Omega \tag{5}$$

$$\frac{{\rm d}s_2}{{\rm d}t} = f_{21} s_1 \sin \Delta\Omega \tag{6}$$

$$\frac{{\rm d}\Omega_1}{{\rm d}t} = -(f_{12} + f_{1{\rm d}}) + f_{12}\frac{s_2}{s_1}\cos \Delta\Omega \tag{7}$$

$$\frac{{\rm d}\Omega_2}{{\rm d}t} = -(f_{21} + f_{2{\rm d}}) + f_{21}\frac{s_1}{s_2}\cos \Delta\Omega, \tag{8}$$

where subscripts 1 and 2 denote the inner and outer planet, $\Delta\varpi = \varpi_2 - \varpi_1$, $\Delta\Omega = \Omega_2 - \Omega_1$, and $s = 2\sin\frac{1}{2}i$. The planet-induced precession frequencies are

$$f_{12} = \frac{G m_1 m_2 a_1}{a_2^2 L_1} b_{3/2}^{(1)}\left(\frac{a_1}{a_2}\right) \tag{9}$$

$$g_{12} = \frac{G m_1 m_2 a_1}{a_2^2 L_1} b_{3/2}^{(2)}\left(\frac{a_1}{a_2}\right) \tag{10}$$

$$f_{21} = \frac{L_1}{L_2} f_{12}, \quad g_{21} = \frac{L_1}{L_2} g_{12}, \tag{11}$$

for gravitational constant G, planet mass m, semimajor axis a (conserved in this secular theory), leading-order angular momentum $L_k = m_k\sqrt{G M_\star a}$, stellar mass $M_\star$, and Laplace coefficient b (Murray & Dermott 2000; Pu & Lai 2018). The disc-induced precession frequency of planet k is

$$f_{k{\rm d}} = \frac{G m_k a_k}{L_k}\int_{r_{\rm in}}^{r_{\rm out}} \frac{2\pi\Sigma(r)}{r} b_{3/2}^{(1)}\left(\frac{a_k}{r}\right){\rm d}r, \tag{12}$$

where we assume the disc's surface density profile follows

$$\Sigma(t, r) = \frac{m_{\rm d}(t)}{\pi r_{\rm out} r}, \tag{13}$$

with a disc mass that decays exponentially with time

$$m_{\rm d}(t) = m_{\rm d0} {\rm e}^{-t/t_{\rm d}}. \tag{14}$$

Note that for now we do not include the back-reaction of the planets onto the disc; this restriction is relaxed in our N-body calculation in Section 2.1.2. The equations are solved using the `scipy.integrate.odeint` integrator in `python`.

Fig. 1 displays an example evolution for two giant planets with $m_1 = 1\,{\rm m_J}$ and $m_2 = 10\,{\rm m_J}$, located at $a_1 = 0.8$ au and $a_2 = 3.2$ au from a star of mass $M_\star = {\rm M}_\odot$. Initial eccentricities and inclinations are $e_{10}, i_{10} = 0.02$, and $e_{20}, i_{20} = 0.1$, and initial longitudes are ϖ_{10}, ϖ_{20}, Ω_{10}, $\Omega_{20} = 0$. For the disc, $m_{\rm d0} = 0.1\,{\rm M}_\odot$, $r_{\rm in} = 4.2$ au, $r_{\rm out} = 150$ au, and $t_{\rm d} = 1$ Myr. Such a $m_{\rm d0}$ value is comparable to disc mass estimates for Class 0/I sources (e.g. Jørgensen et al. 2009; Tobin et al. 2015; Segura-Cox et al. 2018; Andersen et al. 2019), and necessary for a secular resonance crossing for our giant planet parameters. Over the course of the integration, as disc mass $m_{\rm d}$ decreases, we see e_1 and i_1 amplify at the expense of e_2 and i_2. The changes are fastest when $\Delta\varpi \approx \pi$ and $\Delta\Omega \approx \pi$. The apsidal and nodal anti-alignments are prolonged by the matching of frequencies $\dot{\varpi}_1$ with $\dot{\varpi}_2$, and $\dot{\Omega}_1$ with $\dot{\Omega}_2$.

Looking more closely at these precession frequencies, we see from equations (3)–(4) and (7)–(8) that they are each composed of two terms. One contribution to the frequency depends on the degree of misalignment, either $\Delta\varpi$ or $\Delta\Omega$; this planet–planet interaction frequency oscillates rapidly and attains large values, positive or

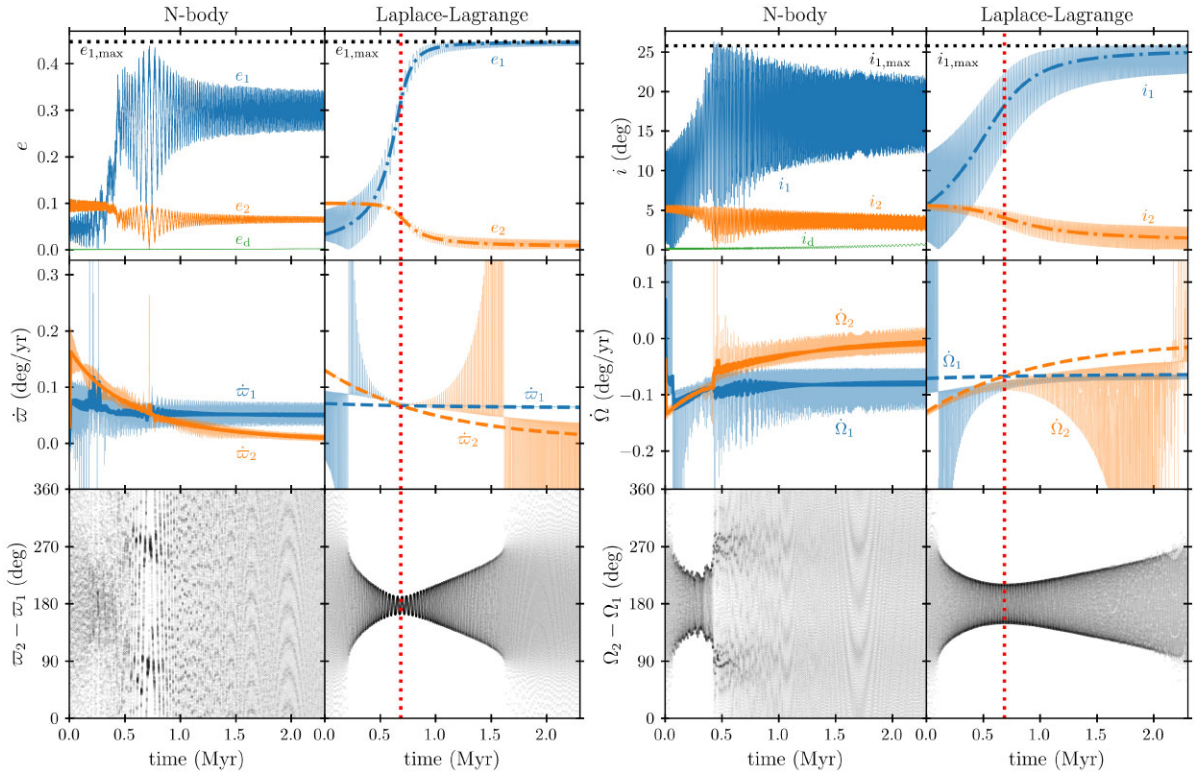

Figure 1. Secular resonance crossing of two planets inside a decaying transition disc, computed with the *N*-body code REBOUND (Rein & Liu 2012), and separately with Laplace–Lagrange theory (equations 1–8). The inner planet's parameters are $\{m_1, a_1, e_{10}, i_{10}\} = \{1\,\mathrm{m_J}, 0.8\,\mathrm{au}, 0.02, 0.02\}$ (with subscript 0 denoting initial conditions, and the reference plane equal to the initial plane of the transition disc), and the outer planet's parameters are $\{m_2, a_2, e_{20}, i_{20}\} = \{10\,\mathrm{m_J}, 3.2\,\mathrm{au}, 0.1, 0.1\}$. Modelled as a point mass in the *N*-body simulation, the disc has $\{m_{\mathrm{d}0}, a_{\mathrm{d}0}\} = \{0.22\,\mathrm{M_\odot}, 14.3\,\mathrm{au}\}$, while in our Laplace–Lagrange treatment, the disc has $\{m_{\mathrm{d}0}, r_{\mathrm{in}}, r_{\mathrm{out}}\} = (0.1\,\mathrm{M_\odot}, 4.2\,\mathrm{au}, 150\,\mathrm{au})$; these parameters yield similar times of resonance crossing when apsides and nodes are anti-aligned ($\Delta\varpi \approx \Delta\Omega \approx 180^\circ$). As computed using Laplace–Lagrange theory, the maximum eccentricity and inclination (equations 21 and 22) of the inner planet are shown as black horizontal dotted lines, while dot–dashed blue and orange lines are solutions from an analytic model for secular resonance passage assuming anti-aligned apses and nodes (the '−' branches of equations A4 and A5). For the *N*-body data on $\dot{\varpi}$ and $\dot{\Omega}$, dark blue and orange curves are time-averaged over a moving window of duration 18 kyr, while for the corresponding Laplace–Lagrange data, dashed curves are non-oscillatory contributions to precession frequencies (equations 15–18). Vertical dotted red lines mark when these non-oscillatory frequencies match and the secular resonance is crossed.

negative, whenever eccentricity or inclination become small. By contrast, the other non-oscillatory frequencies

$$\left.\frac{\mathrm{d}\varpi_1}{\mathrm{d}t}\right|_{\mathrm{non-osc}} = f_{12} + f_{1\mathrm{d}} \tag{15}$$

$$\left.\frac{\mathrm{d}\varpi_2}{\mathrm{d}t}\right|_{\mathrm{non-osc}} = f_{21} + f_{2\mathrm{d}} \tag{16}$$

$$\left.\frac{\mathrm{d}\Omega_1}{\mathrm{d}t}\right|_{\mathrm{non-osc}} = -(f_{12} + f_{1\mathrm{d}}) \tag{17}$$

$$\left.\frac{\mathrm{d}\Omega_2}{\mathrm{d}t}\right|_{\mathrm{non-osc}} = -(f_{21} + f_{2\mathrm{d}}) \tag{18}$$

change much more gradually with time as the outer disc loses mass. These slowly varying frequencies, plotted as dashed curves in Fig. 1, cross at a time marked with a vertical red dotted line. At this moment of 'secular resonance crossing', mean eccentricities and inclinations change fastest.

We can place bounds on how much eccentricities and inclinations grow by examining the constants of motion admitted by equations (1)–(2) and (5)–(6):

$$\frac{1}{2}L_1 e_1^2 + \frac{1}{2}L_2 e_2^2 = \text{constant} \tag{19}$$

$$\frac{1}{2}L_1 s_1^2 + \frac{1}{2}L_2 s_2^2 = \text{constant}. \tag{20}$$

When the outer planet has much more angular momentum than the inner ($L_2 \gg L_1$, as is the case in Fig. 1), the maximum eccentricity and inclination that can be attained by the inner planet depend on the outer planet's initial conditions:

$$e_{1,\max} \simeq \sqrt{\frac{L_2}{L_1}} e_{20} \tag{21}$$

$$i_{1,\max} \simeq 2\sin^{-1}\left(\sqrt{\frac{L_2}{L_1}}\sin\frac{1}{2}i_{20}\right). \tag{22}$$

Fig. 1 demonstrates that e_1 and i_1 come close to their respective maxima after the secular resonance crossing. Appendix A and Section 2.1.3 explore in more detail why $L_2 > L_1$ and passage through anti-aligned states are preferred for inclination and eccentricity excitation.

2.1.2 *N*-body

We solve the same problem as above (two planets inside a decaying outer disc) now using the REBOUND *N*-body code outfitted with the IAS15 integrator (Rein & Spiegel 2015). The outer disc is modelled as a point particle whose mass m_{d} decays exponentially with time constant $t_{\mathrm{d}} = 1\,\mathrm{Myr}$; to effect this, we use the REBOUNDx routine modify_mass (Kostov et al. 2016; Tamayo et al. 2020) setting

mass_loss $= -t_{\rm d}$. The initial disc mass of $0.22\,{\rm M}_\odot$ and initial semimajor axis of $a_{\rm d} = 14.3$ au are chosen to yield a secular resonance crossing time comparable to that in our Laplace–Lagrange solution above ($\sim$0.7 Myr). Modelled as a point particle just like the planets, the disc has an eccentricity $e_{\rm d}$ and inclination $i_{\rm d}$ that are free to vary; in practice they do not deviate much from their initial values of 0, as the disc contains the lion's share of the system's angular momentum (this assumption eventually breaks down as $m_{\rm d}$ decreases to zero, resulting in a slight increase in $e_{\rm d}$ and $i_{\rm d}$ at late times $t \gtrsim 5$ Myr, not plotted).

Fig. 1 shows that the *N*-body solution broadly matches the Laplace–Lagrange solution – e_1 and i_1 increase while e_2 and i_2 decrease as a result of a secular resonance crossing. In the *N*-body evolution, the magnitude of the changes in eccentricity and inclinaton are more muted, apsidal and nodal anti-alignments between planets 1 and 2 are more short-lived, and precession frequencies match only momentarily and not at all after the secular resonance is crossed.

By modelling the disc as a particle in our *N*-body simulation, we neglect how planets excite and interact with waves in the disc (e.g. Goldreich & Tremaine 1980; Tanaka & Ward 2004). Most relevant to our study are long-wavelength apsidal and nodal waves that can exchange angular momentum with a planet (Goldreich & Sari 2003). Our *N*-body particle treatment does allow for angular momentum exchange between the disc and planets, but neglects how that exchange depends on the wave nature of apsidal and nodal disturbances in the disc.

2.1.3 *Parameter space exploration (*N*-body)*

In Fig. 2, we explore how changing the angular momenta of the outer planet + disc (while keeping $L_2 > L_1$) and separately, the disc depletion time, affect the eccentricity and inclination evolution of the inner planet in our *N*-body runs. As the outer bodies' angular momenta are increased, the final i_1 increases as well, respecting $i_{1,\,\rm max}$. A similar trend plays out for e_1. We also see that the excitation of e_1 and i_1 do not much depend on $t_{\rm d}$, presumably as long as the decay time exceeds the secular oscillation periods (e.g. f_{12}^{-1}, f_{2d}^{-1}). Note, however, how the shortest decay times sampled in Fig. 2 yield the largest i_1.

Fig. 3 explores the evolution when the outer planet's initial eccentricity e_{20} and inclination i_{20} are set to higher values. Outcomes are largely the same as before, except for the run where $e_{20} < i_{20}$ (first column), where an eccentricity secular resonance is not encountered, and the final e_1 does not respect $e_{1,\,\rm max}$ as derived from Laplace–Lagrange. What happens instead is that i_1 grows to values $\gtrsim 40^\circ$, large enough for e_1 to trade off with i_1 in a Lidov–Kozai resonance (not captured by Laplace–Lagrange) – see how the periastron argument ω_1 starts to librate near the Kozai fixed points of $\pm 90^\circ$ and eventually locks onto 90°.

We have focused so far on the case where the outer planet has more angular momentum than the inner. We find that when the angular momentum ratio is flipped, the planets do not cross a secular resonance. When $L_1 > L_2$, the planet–planet precession frequencies $f_{12} < f_{21}$ (equation 11). Meanwhile, the planet–disc frequencies satisfy $f_{1\rm d} < f_{2\rm d}$ since the exterior planet lies closer to the cavity edge (equation (12)). Hence, the magnitudes of the non-oscillatory nodal and apsidal precession frequencies of the outer planet, $f_{21} + f_{2\rm d}$, always stay higher than those of the inner planet, $f_{12} + f_{1\rm d}$, and there is never a crossing (equations 15–18). Fig. 4 plots a sample $L_2 < L_1$ integration where $\{m_1, a_1\} = \{10\,{\rm m_J}, 1.6\,{\rm au}\}$ and $\{m_2, a_2\} = \{1\,{\rm m_J}, 3.2\,{\rm au}\}$. The system does not pass into or out of an aligned or anti-aligned state; in this particular example, it starts and stays within an aligned state, and the planet eccentricities and inclinations do not change much. Appendix A explains this result in greater detail.

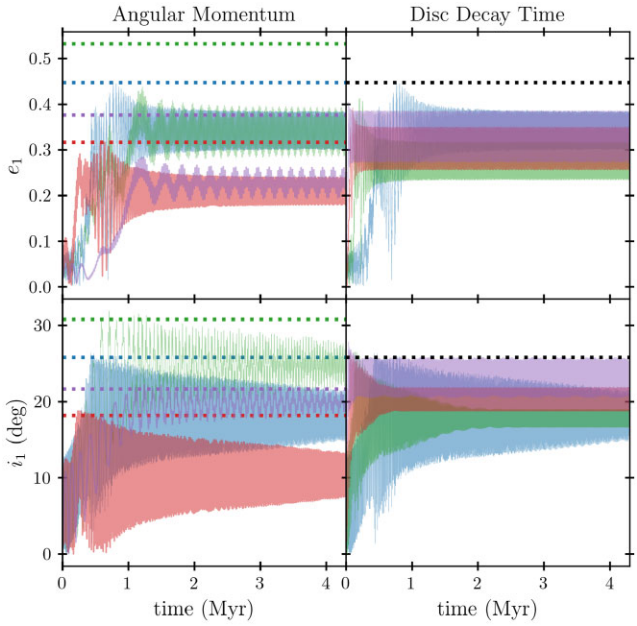

Figure 2. Parameter space exploration for simulations with two planets + a decaying outer disc. All runs shown here use REBOUND, with $\{m_1, a_1\} = \{1\,{\rm m_J}, 0.8\,{\rm au}\}$, $e_{10} = i_{10} = 0.02$, and $e_{20} = i_{20} = 0.1$, the same parameters as in Fig. 1. *Left-hand panels*: effects of varying the angular momentum of the outer planet (and concomitantly the outer disc). In order of increasing angular momentum: $\{m_2, a_2, m_{\rm d0}, a_{\rm d0}\} = \{5\,{\rm m_J}, 3.2\,{\rm au}, 0.20\,{\rm M}_\odot, 17.2\,{\rm au}\}$ (red), $\{5\,{\rm m_J}, 6.4\,{\rm au}, 0.12\,{\rm M}_\odot, 42.8\,{\rm au}\}$ (purple), $\{10\,{\rm m_J}, 3.2\,{\rm au}, 0.22\,{\rm M}_\odot, 14.3\,{\rm au}\}$ (blue), and $\{10\,{\rm m_J}, 6.4\,{\rm au}, 0.14\,{\rm M}_\odot, 35.3\,{\rm au}\}$ (green), with $t_{\rm d} = 1$ Myr. Dotted lines denote $e_{1,\,\rm max}$ and $i_{1,\,\rm max}$ as computed using equations (21) and (22). *Right-hand panels*: effects of varying the disc decay time. In order of decreasing decay time: $t_{\rm d} = 1$ Myr (blue), 0.3 Myr (green), 0.1 Myr (red), and 0.03 Myr (purple), with $\{m_2, a_2, m_{\rm d0}, a_{\rm d0}\} = \{10\,{\rm m_J}, 3.2\,{\rm au}, 0.22\,{\rm M}_\odot, 14.3\,{\rm au}\}$.

2.2 Inner disc and planet in a transition disc cavity

Here, we replace the inner planet of Section 2.1 with a disc. We now have two discs, one interior to a planet and another exterior. Rigid precession of either disc is assumed to be enforced by some collective effect, e.g. bending waves (e.g. Lubow & Ogilvie 2000; Nealon et al. 2018; Zanazzi & Lai 2018a; Zhu 2019) or disc self-gravity (e.g. Zanazzi & Lai 2017; Batygin 2018). As with the outer disc, the inner disc loses mass; the inner disc's angular momentum can become small relative to the planet's, enabling the excitation of large mutual inclination (equation 22). To more accurately model large inclinations, we replace the Laplace–Lagrange equations of Section 2.1.1 with the vector formalism of Lai & Pu (2017), which accounts for how nodal precession rates depend on inclination (see also the appendix of Zanazzi & Lai 2017). These vector equations are designed to model well-separated masses, and are thus appropriately applied to large transition disc cavities far removed from their inner discs (e.g. Francis & van der Marel 2020; Bohn et al. 2022). For simplicity, we fix the eccentricities of all masses to be zero, but account for back-reaction by allowing the outer disc inclination to freely evolve.

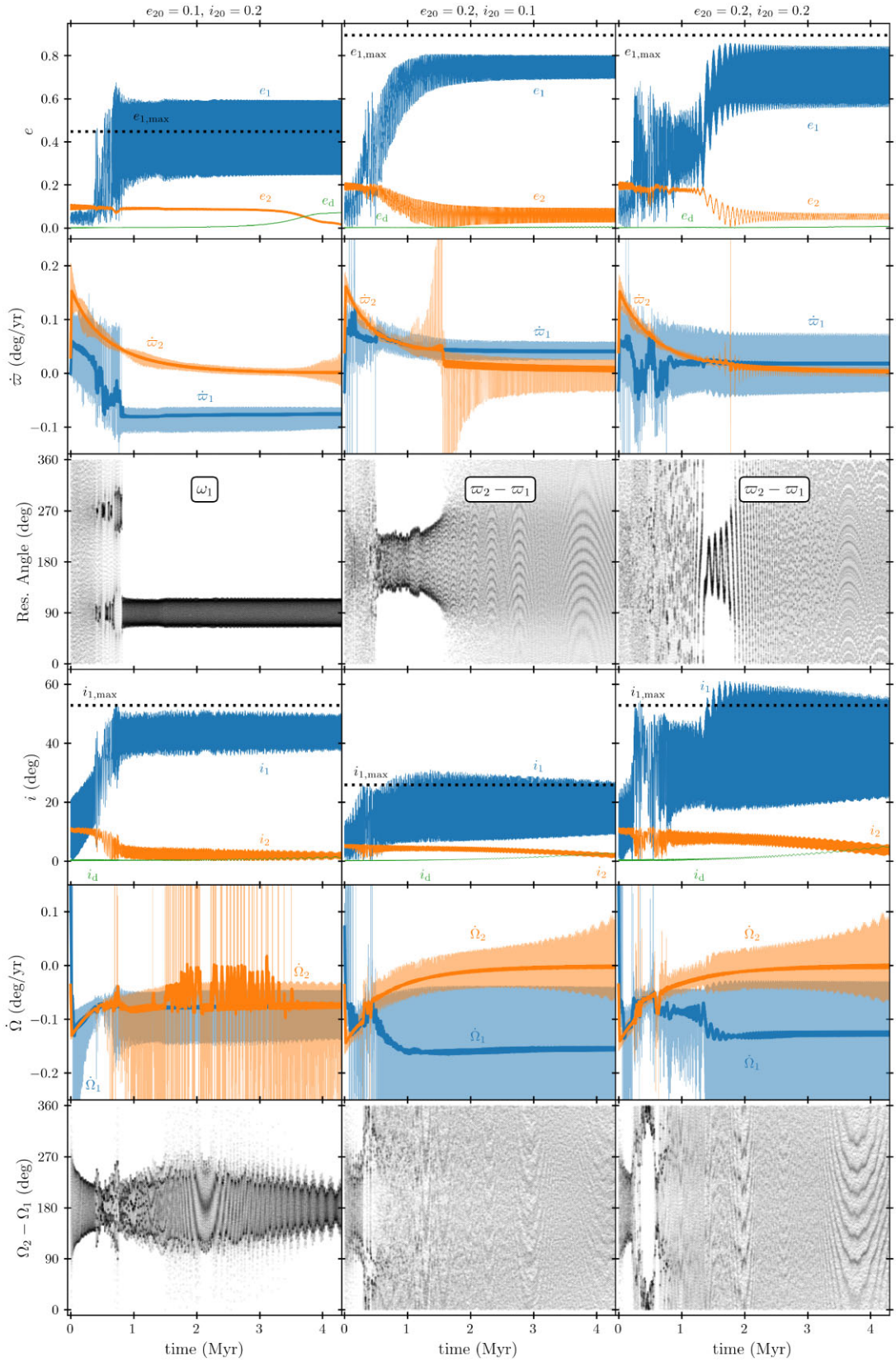

Figure 3. Similar to Fig. 1, showing *N*-body simulations of two planets + a decaying outer disc, and varying the initial eccentricity e_{20}, and initial inclination i_{20} of the outer planet as indicated above each column. Remaining planet and disc parameters are $\{m_1, a_1, m_2, a_2, m_{d0}, a_{d0}\} = \{1\,\mathrm{m_J}, 0.8\,\mathrm{au}, 10\,\mathrm{m_J}, 3.2\,\mathrm{au}, 0.22\,\mathrm{M_\odot}, 14.3\,\mathrm{au}\}$ and $i_{10} = e_{10} = 0.02$. In the left column, the system captures into the Lidov–Kozai resonance where the argument of pericentre $\omega_1 = \varpi_1 - \Omega_1$ librates about 90°, and e_1 does not respect $e_{1,\max}$ as given by (21) from Laplace–Lagrange theory.

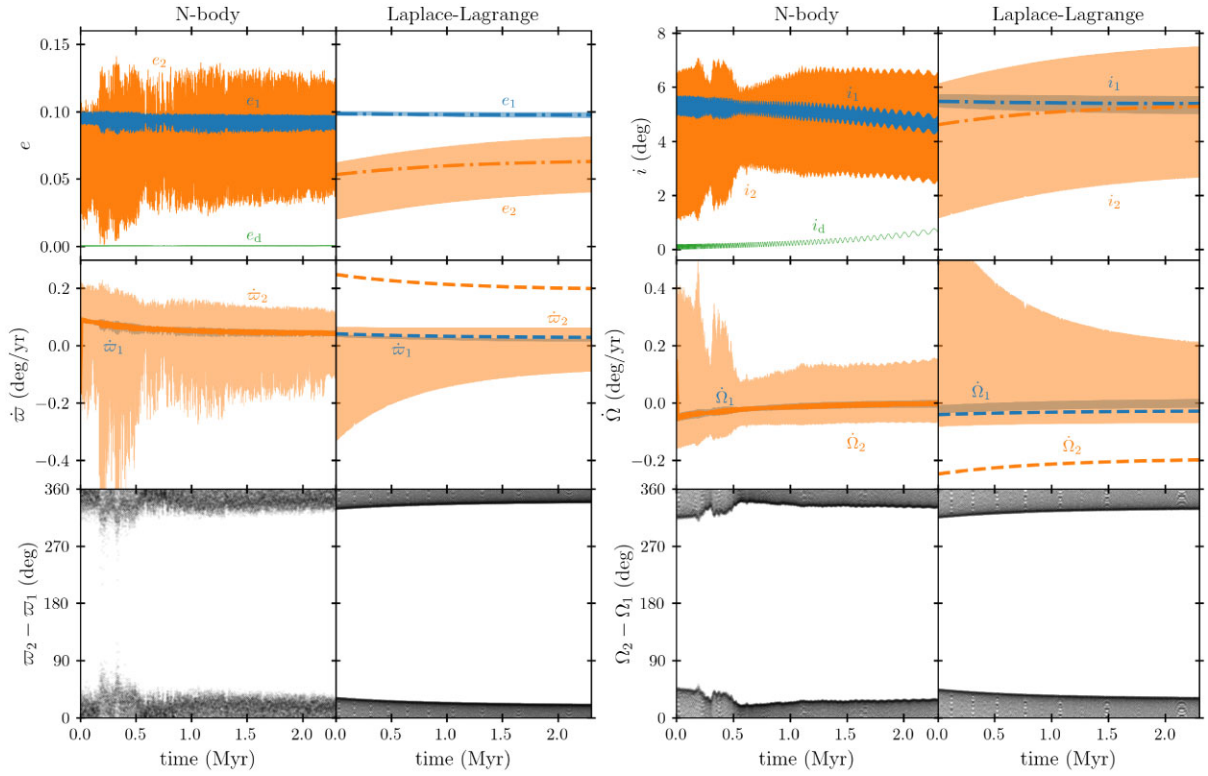

Figure 4. Similar to Fig. 1, showing simulations of two planets + a decaying outer disc, but now with the outer planet having less angular momentum than the inner: $\{m_1, a_1, m_2, a_2\} = \{10\,\mathrm{mJ}, 1.6\,\mathrm{au}, 1\,\mathrm{mJ}, 3.2\,\mathrm{au}\}$. Initial eccentricities and inclinations are $e_{10} = i_{10} = 0.1$ and $e_{20} = i_{20} = 0.02$, and disc parameters are identical to those in Fig. 1. In the Laplace–Lagrange solution, the non-oscillatory precession frequencies of the two planets never match (dashed curves; equations (15)–18), no secular resonance is crossed, and eccentricities and inclinations do not undergo large changes aside from the outer planet's secular oscillations. A qualitatively similar evolution plays out in the *N*-body calculation. Note how the planets are apsidally and nodally aligned from start to finish but do not much change their eccentricities or inclinations; see Appendix A.

The orbit normals of the inner disc ($\hat{\boldsymbol{l}}_1$), planet ($\hat{\boldsymbol{l}}_\mathrm{p}$), and outer disc ($\hat{\boldsymbol{l}}_2$) obey:

$$\frac{\mathrm{d}\hat{\boldsymbol{l}}_1}{\mathrm{d}t} = f_{1\mathrm{p}}(\hat{\boldsymbol{l}}_1\cdot\hat{\boldsymbol{l}}_\mathrm{p})(\hat{\boldsymbol{l}}_1\times\hat{\boldsymbol{l}}_\mathrm{p}) + f_{12}(\hat{\boldsymbol{l}}_1\cdot\hat{\boldsymbol{l}}_2)(\hat{\boldsymbol{l}}_1\times\hat{\boldsymbol{l}}_2) \tag{23}$$

$$\frac{\mathrm{d}\hat{\boldsymbol{l}}_\mathrm{p}}{\mathrm{d}t} = f_{\mathrm{p}1}(\hat{\boldsymbol{l}}_\mathrm{p}\cdot\hat{\boldsymbol{l}}_1)(\hat{\boldsymbol{l}}_\mathrm{p}\times\hat{\boldsymbol{l}}_1) + f_{\mathrm{p}2}(\hat{\boldsymbol{l}}_\mathrm{p}\cdot\hat{\boldsymbol{l}}_2)(\hat{\boldsymbol{l}}_\mathrm{p}\times\hat{\boldsymbol{l}}_2) \tag{24}$$

$$\frac{\mathrm{d}\hat{\boldsymbol{l}}_2}{\mathrm{d}t} = f_{21}(\hat{\boldsymbol{l}}_2\cdot\hat{\boldsymbol{l}}_1)(\hat{\boldsymbol{l}}_2\times\hat{\boldsymbol{l}}_1) + f_{2\mathrm{p}}(\hat{\boldsymbol{l}}_2\cdot\hat{\boldsymbol{l}}_\mathrm{p})(\hat{\boldsymbol{l}}_2\times\hat{\boldsymbol{l}}_\mathrm{p}). \tag{25}$$

The precession frequencies are given by:

$$f_{1\mathrm{p}} = \frac{1}{L_1}\int_{r_{1,\mathrm{in}}}^{r_{1,\mathrm{out}}} \frac{2\pi G\Sigma_1 m_\mathrm{p} r_1^2}{a_\mathrm{p}^2} b_{3/2}^{(1)}\left(\frac{r_1}{a_\mathrm{p}}\right)\mathrm{d}r_1 \tag{26}$$

$$f_{\mathrm{p}2} = \frac{1}{L_\mathrm{p}}\int_{r_{2,\mathrm{in}}}^{r_{2,\mathrm{out}}} \frac{2\pi G\Sigma_2 m_\mathrm{p} a_\mathrm{p}}{r_2} b_{3/2}^{(1)}\left(\frac{a_\mathrm{p}}{r_2}\right)\mathrm{d}r_2 \tag{27}$$

$$f_{12} = \frac{1}{L_1}\int_{r_{2,\mathrm{in}}}^{r_{2,\mathrm{out}}}\int_{r_{1,\mathrm{in}}}^{r_{1,\mathrm{out}}} \frac{4\pi^2 G\Sigma_1\Sigma_2 r_1^2}{r_2} b_{3/2}^{(1)}\left(\frac{r_1}{r_2}\right)\mathrm{d}r_1\mathrm{d}r_2 \tag{28}$$

$$f_{\mathrm{p}1} = \frac{L_1}{L_\mathrm{p}} f_{1\mathrm{p}}, \quad f_{2\mathrm{p}} = \frac{L_\mathrm{p}}{L_2} f_{\mathrm{p}2}, \quad f_{21} = \frac{L_1}{L_2} f_{12}, \tag{29}$$

where the inner disc of radial coordinate r_1 extends from $r_{1,\mathrm{in}}$ to $r_{1,\mathrm{out}}$, and similarly for the outer disc. The planet's angular momentum (to leading order) is $L_\mathrm{p} = m_\mathrm{p}\sqrt{GM_\star a_\mathrm{p}}$ for planet mass m_p and semimajor axis a_p, stellar mass $M_\star$, and gravitational constant G. The inner and outer disc surface density profiles are assumed to follow:

$$\Sigma_1(t, r_1) = \frac{m_1(t)}{2\pi r_{1,\mathrm{out}} r_1}, \quad \Sigma_2(t, r_2) = \frac{m_2(t)}{2\pi r_{2,\mathrm{out}} r_2} \tag{30}$$

for disc masses

$$m_1(t) = \delta\frac{r_{1,\mathrm{out}}}{r_{2,\mathrm{out}}} m_2(t), \quad m_2(t) = m_{20}\mathrm{e}^{-t/t_\mathrm{d}}, \tag{31}$$

where δ is a free parameter that measures how much lower the inner disc surface density is relative to the outer (where the latter is extrapolated to the same inner disc radius; see section 3.3 and fig. 5 of Francis & van der Marel 2020). For $r_{1,\,\mathrm{in}} \ll r_{1,\,\mathrm{out}}$ and $r_{2,\,\mathrm{in}} \ll r_{2,\,\mathrm{out}}$, the (leading-order) disc angular momenta are:

$$L_1(t) = \frac{2}{3} m_1(t)\sqrt{GM_\star r_{1,\mathrm{out}}} \tag{32}$$

$$L_2(t) = \frac{2}{3} m_2(t)\sqrt{GM_\star r_{2,\mathrm{out}}}. \tag{33}$$

Fig. 5 plots three sample integrations of equations (23)–(25) for different choices of $a_\mathrm{p} = \{12, 20\}$ au and $\delta = \{2\times10^{-3}, 2\times10^{-2}\}$, values motivated by observations of material inside the cavities of transitional discs (e.g. Ubeira Gabellini et al. 2019; Francis & van der Marel 2020; Portilla-Revelo et al. 2023). The annular extent of the inner disc is taken to be $\{r_{1,\mathrm{in}}, r_{1,\mathrm{out}}\} = \{0.03, 5\}$ au, and for the outer disc $\{r_{2,\mathrm{in}}, r_{2,\mathrm{out}}\} = \{30, 200\}$ au. In all cases, the inner and outer discs are assumed initially co-planar, and the planet has an initial seed inclination of $i_{\mathrm{p}0} = 3^\circ$. We see that i_1 amplifies when the

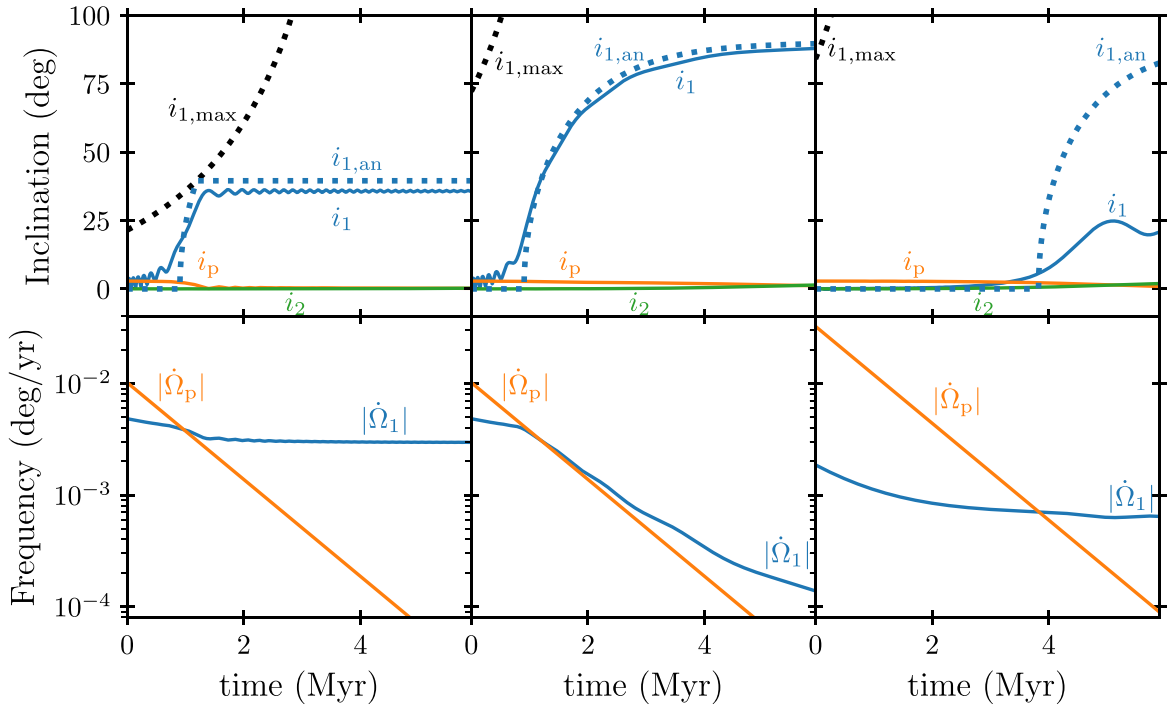

Figure 5. Secular evolution of a planet (subscript p) sandwiched between a decaying inner disc (subscript 1) and decaying exterior disc (subscript 2), calculated using the vector equations of Section 2.2. Parameters are $\{t_\mathrm{d}, m_{20}, m_\mathrm{p}, r_{1,\mathrm{in}}, r_{1,\mathrm{out}}, r_{2,\mathrm{in}}, r_{2,\mathrm{out}}\} = \{1\,\mathrm{Myr}, 0.2\,\mathrm{M}_\odot, 5\,\mathrm{m_J}, 0.03\,\mathrm{au}, 5\,\mathrm{au}, 30\,\mathrm{au}, 200\,\mathrm{au}\}$, with each column corresponding to $\{a_\mathrm{p}, \delta\} = \{12\,\mathrm{au}, 2\times10^{-2}\}$ (left), $\{12\,\mathrm{au}, 2\times10^{-3}\}$ (middle), and $\{20\,\mathrm{au}, 2\times10^{-3}\}$ (right), respectively, where $\delta \equiv (m_1/m_2)(r_{2,\mathrm{out}}/r_{1,\mathrm{out}})$ (equation 31; see also fig. 9 of Francis & van der Marel 2020 for observationally inferred values of δ). The analytic prediction for the inner disc inclination $i_{1,\mathrm{an}}$ (equation 36 and text below equation (38)) agrees well with the numerically computed i_1, except for the simulation in the right column where secular resonance ($\dot\Omega_1 \approx \dot\Omega_\mathrm{p}$) cannot be maintained because the planet's angular momentum exceeds that of the outer disc.

nodal precession rate of the inner disc:

$$\dot\Omega_1 \simeq -f_{1\mathrm{p}}\cos i_1 - f_{12}\cos i_1 \tag{34}$$

matches that of the planet:

$$\dot\Omega_\mathrm{p} \simeq -f_{\mathrm{p}1}\cos i_1 - f_{\mathrm{p}2}, \tag{35}$$

where we have taken the reference plane to be perpendicular to the initial $\hat{\boldsymbol{l}}_2$, approximated $\hat{\boldsymbol{l}}_\mathrm{p}$ and $\hat{\boldsymbol{l}}_2$ to be constant and nearly parallel (as Fig. 5 confirms), and kept only the non-oscillatory contributions to the frequencies (dropping the dependence of $\dot\Omega_1$ and $\dot\Omega_\mathrm{p}$ on the relative nodes). The nodal frequencies $\dot\Omega_1$ and $\dot\Omega_\mathrm{p}$ can track one another for some time; see especially the middle column of Fig. 5. Setting $\dot\Omega_1 = \dot\Omega_\mathrm{p}$ gives an analytic estimate for i_1 during resonance lock:

$$\cos i_{1,\mathrm{an}} \approx \frac{f_{2\mathrm{p}}}{f_{1\mathrm{p}} - f_{\mathrm{p}1} + f_{12}}. \tag{36}$$

As $f_{2\mathrm{p}} \to 0$, $i_{1,\mathrm{an}} \to 90^\circ$ (Petrovich et al. 2020).

We can also derive a maximum i_1 as we did in Section 2.1. From equations (23) and (24) and $\mathrm{d}\hat{\boldsymbol{l}}_2/\mathrm{d}t = 0$ (back-reaction on the outer disc neglected), we have

$$L_1(1-\cos i_1) + L_\mathrm{p}(1-\cos i_\mathrm{p}) \simeq \text{constant} \tag{37}$$

which yields

$$i_{1,\max} \simeq 2\sin^{-1}\left(\sqrt{\frac{L_\mathrm{p}}{L_1}}\sin\frac{1}{2}i_{\mathrm{p}0}\right) \tag{38}$$

when $L_1 \ll L_\mathrm{p}$. This result is identical to equation (22) as derived using Laplace–Lagrange. Equation (36) holds when $f_{2\mathrm{p}} < f_{1\mathrm{p}} - f_{\mathrm{p}1} + f_{12}$ and $i_{1,\mathrm{an}} < i_{1,\max}$. We can piece together a more complete analytic solution for i_1 by setting $i_{1,\mathrm{an}} = 0$ when $f_{2\mathrm{p}} \geq f_{1\mathrm{p}} - f_{\mathrm{p}1} + f_{12}$, and further setting $i_{1,\mathrm{an}}(t) = i_{1,\max}(t_\mathrm{c})$, where t_c is the time when $i_{1,\mathrm{an}}$ first crosses $i_{1,\max}$. We see from Fig. 5 that $i_{1,\mathrm{an}}$ so constructed agrees well with the full solutions shown in the left and middle columns. If the planet's angular momentum exceeds that of the outer disc when secular resonance is first encountered (i.e. if $L_\mathrm{p} \gtrsim L_2$ when $\dot\Omega_1 \approx \dot\Omega_p$), secular resonance locks cannot be sustained, and equation (36) is a poor predictor of i_1 (right column).

One can rearrange equation (38) to estimate the minimum planet mass required to tilt the inner disc:

$$m_\mathrm{p} > m_{\mathrm{p,min}} = \frac{2}{3}m_1\left(\frac{r_{1,\mathrm{out}}}{a_\mathrm{p}}\right)^{1/2}\frac{\sin^2\frac{1}{2}i_{1,\max}}{\sin^2\frac{1}{2}i_{\mathrm{p}0}}. \tag{39}$$

Fig. 6 plots $m_{\mathrm{p,min}}$ as a function of a_p and m_1. Take for example an inner disc having mass $m_1 \gtrsim 0.01\,\mathrm{m_J}$ on scales of $r_{1,\mathrm{out}} = 5\,\mathrm{au}$. A planet at $a_\mathrm{p} = 10$–$50\,\mathrm{au}$ with mass $m_\mathrm{p} \gtrsim 0.3\,\mathrm{m_J}$ can tilt such an inner disc from 3° to 30°, provided they are surrounded by an outer disc dominating the angular momentum budget.

3 EXTENSIONS

3.1 Forming inclined, apsidally-orthogonal planetary systems

Dawson & Chiang (2014, hereafter DC14) identified a subset of warm Jupiters whose sky-projected arguments of pericentre $\omega_{\mathrm{sky},1}$ differed from those of their exterior giant-planet companions by $|\Delta\omega_\mathrm{sky}| \equiv |\omega_{\mathrm{sky},1} - \omega_{\mathrm{sky},2}| \approx 90^\circ$. Although ω_sky is technically a sky-projected angle (between the orbit's eccentricity vector and the

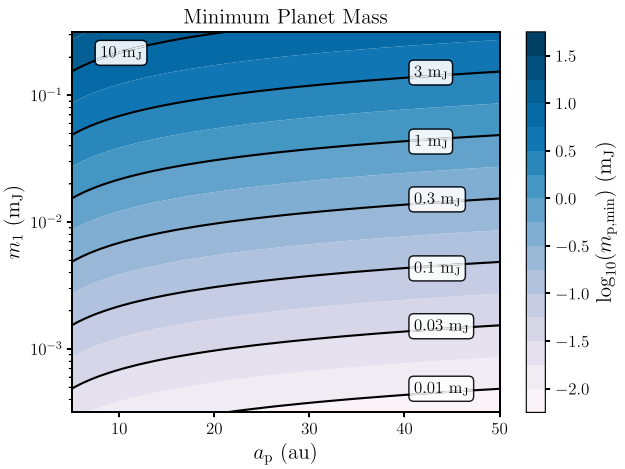

Figure 6. Minimum planet mass $m_{\rm p,min}$ required to tilt the inner disc by $i_{1,\rm max} = 30^\circ$ (equation 39), as a function of the inner disc mass m_1 and the planet semimajor axis $a_{\rm p}$, assuming $\{r_{1,\rm out}, i_{\rm p0}\} = \{5\,{\rm au}, 3^\circ\}$. See also Fig. 12, which shows that this minimum planet mass satisfies observational constraints in the transition disc hosted by CQ Tau.

vector from the star to the orbit's ascending node on the sky plane; see, e.g. fig. 1 of Chiang, Tabachnik & Tremaine 2001), DC14 found that $|\Delta\omega_{\rm sky}|$ is a good proxy for $|\Delta\varpi| = |\varpi_2 - \varpi_1|$, the angle between the eccentricity vectors of two orbits. Thus, $|\Delta\omega_{\rm sky}| \approx 90^\circ$ points to planet pairs with near-orthogonal apsides. Such pairs were argued by DC14 to have mutual inclinations of $\sim 40^\circ$, in contrast to apsidally-aligned ($|\Delta\omega_{\rm sky}| \approx 0^\circ$) and anti-aligned ($|\Delta\omega_{\rm sky}| \approx 180^\circ$) pairs argued to be more nearly co-planar (e.g. Chiang, Tabachnik & Tremaine 2001; Nagasawa, Lin & Ida 2003; Petrovich, Wu & Ali-Dib 2019).

Fig. 7 updates fig. 1 of DC14, showing $|\Delta\omega_{\rm sky}|$ for systems known to have two (and only two) planets with measured radial velocities or transit timing variations, taken from the NASA Exoplanet Archive (77 per cent), the Exoplanet Encyclopedia (18 per cent), and the Exoplanet Orbit Database (5 per cent). The clustering of systems with $|\Delta\omega_{\rm sky}| \approx 90^\circ$ noted by DC14 is no longer apparent.[2] The histogram of $|\Delta\omega_{\rm sky}|$ on the right-hand panel shows a fairly smooth continuum, with a mild preference for apsidal alignment over anti-alignment by a factor of $\sim$2–3.

What mutual inclinations do these $|\Delta\omega_{\rm sky}|$'s imply? To investigate this question, we integrate the secular equations of motion for two eccentric planets, systematically varying the initial mutual inclination $i_{\rm mut,\,0}$ and examining its effect on the phase-mixed distributions of $\Delta\varpi = |\varpi_2 - \varpi_1|$ (which we use as a proxy for $\Delta\omega_{\rm sky}$, following DC14). We use equations (17)–(20) of Liu, Muñoz & Lai (2015), which can accommodate large eccentricities and inclinations and incorporate general relativistic precession for the inner planet (e.g. Eggleton & Kiseleva-Eggleton 2001). Parameters/initial conditions are chosen to be representative of giant planet pairs with radial velocity data: $\{m_1, a_1, e_{10}\} = \{1\,{\rm m_J}, 0.2\,{\rm au}, 0.3\}$, $\{m_2, a_2, e_{20}\} = \{3\,{\rm m_J}, 1.0\,{\rm au}, 0.3\}$, $\Omega_{20} - \Omega_{10} = 180^\circ$, and ω_{10} and ω_{20} drawn uniformly from 0 to 2π.

The distributions of $|\Delta\varpi|$ after 1 Myr, parametrized by $i_{\rm mut,\,0}$, are shown in Fig. 8. We see that the $|\Delta\varpi|$ distributions corresponding to nearly co-planar systems, having a factor-of-2 preference for alignment over anti-alignment when $i_{\rm mut,\,0} \lesssim 20^\circ$, seem to fit the observed distribution of $|\Delta\omega_{\rm sky}|$ (as shown in Fig. 7) best. We conclude that the statistical evidence presented by DC14 for a population of highly inclined, apsidally-orthogonal giant-planet pairs no longer exists.

None the less, it is still possible that a given individual system observed today to be apsidally orthogonal has a $\sim 40^\circ$ mutual inclination, following the dynamics described by DC14 whereby $|\Delta\omega_{\rm sky}|$ lingers near 90° as it oscillates about 180°. We now ask whether the large mutual inclination presumed for such configurations may have originated from a secular resonance crossing driven by a decaying outer disc. We take as a case study, one of the systems highlighted by DC14, HD 147018. To decide whether a crossing may have occurred, we literally integrate the system *backwards* in time, starting the calculation at $t = 8\,{\rm Myr}$ (the present day), ending at $t = 0$, and prescribing the outer disc to *increase* up to a mass of $m_{\rm d0} = 0.5\,{\rm M_\odot}$. The disc is otherwise modelled the same way as in Section 2.1, for assumed parameters $r_{\rm in} = 3.3\,{\rm au}$, $r_{\rm out} = 150\,{\rm au}$, and $t_{\rm d} = 1\,{\rm Myr}$. We have verified that the system is time-reversible by integrating forwards and backwards and achieving consistent results. We use again Liu, Muñoz & Lai (2015) to model the secular interaction of two planets and include general relativistic precession for the inner planet. The contributions to planet precession from the disc are given by:

$$\left.\frac{{\rm d}\boldsymbol{j}_k}{{\rm d}t}\right|_{kd} = f_{kd}\boldsymbol{j}_k \times \hat{\boldsymbol{l}}_{\rm d} \tag{40}$$

$$\left.\frac{{\rm d}\boldsymbol{e}_k}{{\rm d}t}\right|_{kd} = -f_{kd}\left(2\boldsymbol{e}_k \times \boldsymbol{j}_k - \boldsymbol{e}_k \times \hat{\boldsymbol{l}}_{\rm d}\right) \tag{41}$$

(e.g. Pu & Lai 2018; Petrovich, Wu & Ali-Dib 2019). Here, $\hat{\boldsymbol{l}}$ is the unit-vector orbit normal (subscript d for disc, and k for planet k), $\boldsymbol{e}$ is the eccentricity vector of magnitude e pointing in the direction of pericentre, and $\boldsymbol{j} = \sqrt{1-e^2}\hat{\boldsymbol{l}}$. The frequency f_{kd} is given by equation (12), $f_{dk} = (L_k/L_{\rm d})f_{kd}$, $L_k = m_k\sqrt{GM_\star a_k}$, and $L_{\rm d} = (2/3)m_{\rm d}\sqrt{GM_\star r_{\rm out}}$. The disc evolves according to:

$$\frac{{\rm d}\hat{\boldsymbol{l}}_{\rm d}}{{\rm d}t} = f_{\rm d1}\hat{\boldsymbol{l}}_{\rm d} \times \boldsymbol{j}_1 + f_{\rm d2}\hat{\boldsymbol{l}}_{\rm d} \times \boldsymbol{j}_2. \tag{42}$$

Fig. 9 displays the results of the back-integration of HD 147018, assumed to have a present-day mutual inclination of $i_{\rm mut} = 39^\circ$. The system may indeed have once crossed a secular resonance that increased $i_{\rm mut}$ by a factor of $\sim$3. In this scenario, the inclination i_2 of the outer planet needs to have been $\sim$10–15° in the past; this value agrees with that estimated by inverting equation (22):

$$i_{20,\rm est} \simeq 2\sin^{-1}\left(\sqrt{\frac{L_1}{L_2}}\sin\frac{1}{2}i_{\rm mut}\right) \approx 12^\circ \tag{43}$$

shown as a dashed line in Fig. 9 for $i_{\rm mut} = 39^\circ$. By contrast, the eccentricities do not change as much; e_1 in the past needs to have been about as large as its present-day value of 0.47. Thus, our scenario of a decaying outer disc does not explain the origin of the large eccentricities in HD 147018.

[2] DC14 drew the data for their fig. 1 from the Exoplanet Orbit Database (EOD) only; the systems they highlighted as apsidally orthogonal are shown in red in Fig. 7, with updated parameters. When we also restrict our sample to the EOD, we see evidence for the same clustering of $|\Delta\omega_{\rm sky}|$ near 90° that they reported. It is only when we add the data from the NASA Exoplanet Archive and the Exoplanet Encyclopedia that the clustering goes away.

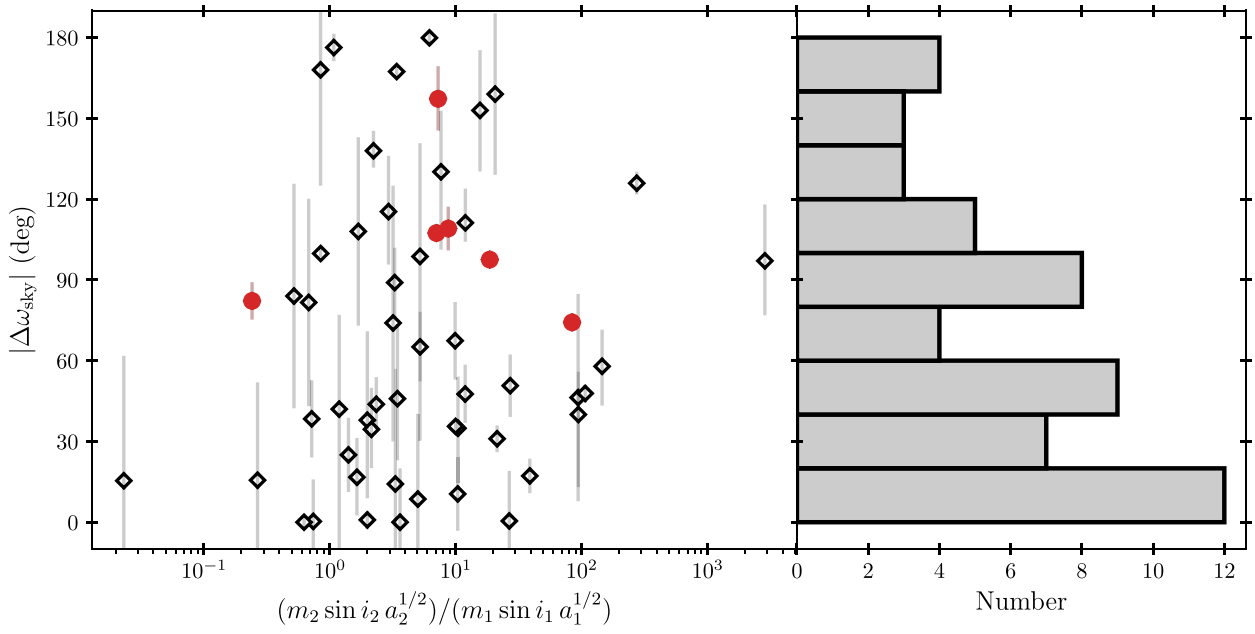

Figure 7. The degree of apsidal alignment in two-planet systems with radial velocity or transit timing data, as measured by the difference in sky-projected arguments of pericentre, $|\Delta\omega_{\rm sky}| = |\omega_{\rm sky,\,1} - \omega_{\rm sky,\,2}|$. Data are taken from the NASA Exoplanet Archive, Exoplanet Encyclopedia, and Exoplanet Orbit Database, selecting only systems where eccentricities are larger than zero with greater than 2σ confidence, and one-sided 1σ errors on $\omega_{\rm sky,}$ are less than 40° (similar cuts were made by Dawson & Chiang 2014). No cut on planet mass or semimajor axis is made for this figure, but we have verified that our conclusions are unchanged if we consider only giant planets, or if we include only planets with $a > 0.1$ au to exclude hot Jupiters (data not shown). The six red points are the same six warm Jupiter systems proposed by Dawson & Chiang (2014) to constitute a distinct class of apsidally misaligned ($|\Delta\omega_{\rm sky}| \approx 90°$), highly inclined pairs. The data as a whole no longer support such a claim, as can be seen in the histogram of $|\Delta\omega_{\rm sky}|$ on the right, which shows no obvious clustering around $|\Delta\omega_{\rm sky}| \approx 90°$, and instead appears more consistent with most if not all pairs having small mutual inclinations – compare with Fig. 8.

3.2 Stellar spin

We consider here how accounting for the host stellar spin and quadrupole moment changes the dynamics of secular resonance crossing. Mostly, we find that it does not fit our parameter space.

3.2.1 Star + planet interactions

For a planet to substantively tilt the spin axis of a star, at least two conditions need to be satisfied. First, the planet's orbital angular momentum $L_{\rm p} = m_{\rm p}\sqrt{GM_\star a_{\rm p}}$ should be larger than the stellar spin angular momentum $S = k_\star M_\star R_\star^2 \Omega_\star$. For our parameters,

$$\frac{S}{L_{\rm p}} = 1.1 \left(\frac{1\,{\rm m_J}}{m_{\rm p}}\right)\left(\frac{1\,{\rm au}}{a_{\rm p}}\right)^{1/2}\left(\frac{3\,{\rm d}}{P_\star}\right)\left(\frac{M_\star}{1\,{\rm M_\odot}}\right)^{1/2}\left(\frac{R_\star}{2\,R_\odot}\right)^2, \quad (44)$$

where $\Omega_\star = 2\pi/P_\star$ is the star's rotation frequency, $P_\star$ is the star's rotation period, and the angular momentum constant $k_\star \simeq 0.2$ for a fully convective body (e.g. Chandrasekhar 1939; Lai, Rasio & Shapiro 1993). For $a_{\rm p} \lesssim 1$ au, $S \gtrsim L_{\rm p}$ and the planet cannot control the star's tilt. For $a_{\rm p} \gtrsim 1$ au, we run up against the second condition that the precession frequency of the star driven by the planet

$$f_{\star{\rm p}} = 2.2 \times 10^{-5} \left(\frac{3\,{\rm d}}{P_\star}\right)\left(\frac{m_{\rm p}}{1\,{\rm m_J}}\right)\left(\frac{1\,{\rm au}}{a_{\rm p}}\right)^3 {\rm deg\,yr^{-1}} \quad (45)$$

be shorter than the precession frequency of the planet; otherwise the planet orbit normal would vary too rapidly to coherently tilt the stellar spin axis (e.g. Lai 2014; Zanazzi & Lai 2018b). In evaluating $f_{\star{\rm p}}$, we have taken the star's second gravitational moment to be $J_2 = k_q \Omega_\star^2/(GM_\star/R_\star^3)$, with $k_q \simeq 0.09$ (e.g. Lai, Rasio & Shapiro 1993).

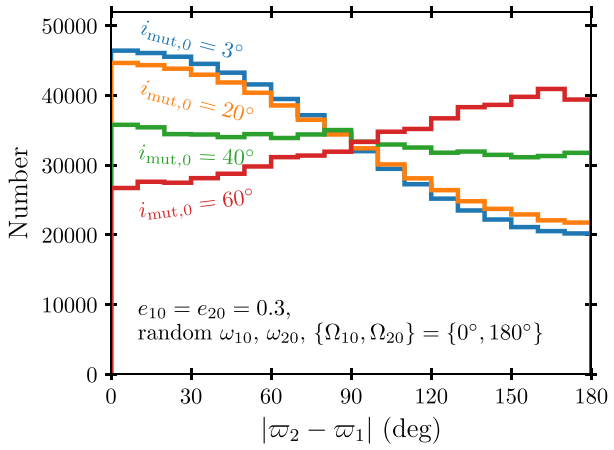

Figure 8. The distribution of $|\Delta\varpi| = |\varpi_2 - \varpi_1|$ sampled from 200 two-planet systems, integrated using eqs. (17)–(20) of Liu, Muñoz & Lai (2015) over 1 Myr. The inner planet has $\{m_1, a_1\} = \{1\,{\rm m_J}, 0.2\,{\rm au}\}$ and the outer planet has $\{m_2, a_2\} = \{3\,{\rm m_J}, 1.0\,{\rm au}\}$. Initial mutual inclinations are as labelled, with initial nodes Ω_{10} and Ω_{20} anti-aligned, initial arguments of pericentre drawn randomly over the interval $[0, 2\pi]$, and initial eccentricities set to 0.3. For $i_{\rm mut,\,0} \lesssim 20°$, the $\Delta\varpi$ distribution decreases monotonically from alignment to anti-alignment in a way that resembles the observed distribution of $|\Delta\omega_{\rm sky}|$ shown in Fig. 7.

For our parameters, typical values of $\dot{\Omega}_{\rm p}$ (see Figs 1 and 3 for $\dot{\Omega}_1$ and $\dot{\Omega}_2$) exceed $f_{\star{\rm p}}$.

What about the converse torque exerted by the oblate star on the planet, conceivably important when $S > L_{\rm p}$? The planet's precession

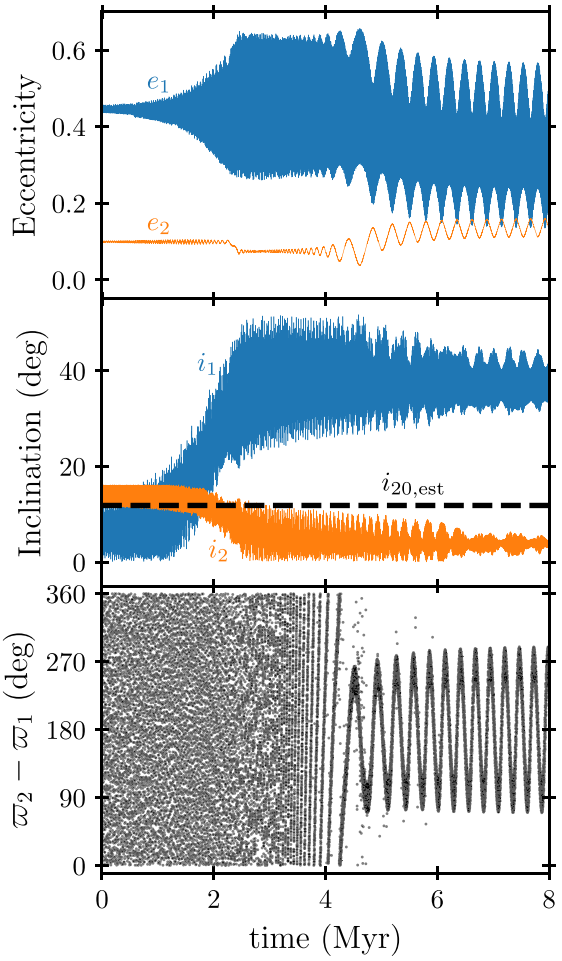

Figure 9. The mutual inclination between HD 147018b and c hypothesized by DC14 to be $\sim 39^\circ$ today could have arisen from a secular resonance crossing driven by a decaying outer disc. The evolution shown is the result of a backwards-integration starting at $t = 8\,\mathrm{Myr}$ with 'initial' conditions from DC14 – $\{M_\star, m_1, m_2, a_1, a_2, e_{1\mathrm{f}}, e_{2\mathrm{f}}, i_{1\mathrm{f}}, i_{2\mathrm{f}}, \omega_{1\mathrm{f}}, \omega_{2\mathrm{f}}, \Omega_{1\mathrm{f}}, \Omega_{2\mathrm{f}}\}$ $= \{0.92\,\mathrm{M}_\odot, 2.1\,\mathrm{m_J}, 6.6\,\mathrm{m_J}, 0.24\,\mathrm{au}, 1.9\,\mathrm{au}, 0.47, 0.13, 35.6^\circ, 3.4^\circ, 66^\circ, 136.9^\circ, 0^\circ, 180^\circ\}$ – augmented with a disc of mass $m_\mathrm{d} = 0.5\,\mathrm{M}_\odot \exp(-t/t_\mathrm{d})$ and having parameters $\{r_\mathrm{in}, r_\mathrm{out}, t_\mathrm{d}\} = \{3.3\,\mathrm{au}, 150\,\mathrm{au}, 1\,\mathrm{Myr}\}$. The system may have originated with a mutual inclination of $i_{20,\,\mathrm{est}} \approx 12^\circ$ (equation 43), crossed a secular resonance that amplified i_1 at the expense of i_2, and settled into apsidal libration with $\Delta\varpi = \varpi_2 - \varpi_1$ lingering near $\pm 90^\circ$ (DC14). However, this formation scenario does not explain the origin of the eccentricities in HD 147018b and c, which do not change much from their large present-day values.

frequency forced by the star is:

$$f_{\mathrm{p}\star} = 2.4\times10^{-5}\left(\frac{3\,\mathrm{d}}{P_\star}\right)^2\left(\frac{1\,\mathrm{au}}{a_\mathrm{p}}\right)^{7/2}\left(\frac{M_\star}{1\,\mathrm{M}_\odot}\right)^{1/2}\left(\frac{R_\star}{1\,R_\odot}\right)^2 \mathrm{deg\,yr^{-1}}. \tag{46}$$

For $a_\mathrm{p} \gtrsim 0.1\,\mathrm{au}$, $f_{\mathrm{p}\star}$ is lower than precession frequencies driven by planet–planet interactions (see, e.g. ϖ, Ω in Figs 1 and 3). Thus the planets generally affect one another more than they are affected by the star.

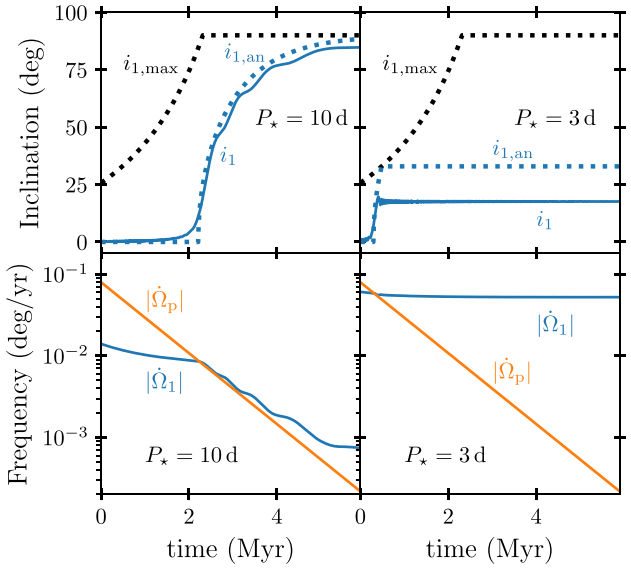

Figure 10. Similar to Fig. 5 showing the secular evolution of an inner disc + planet + outer disc, but now including the torque from the star's mass quadrupole for the stellar rotation periods $P_\star$ indicated. Other model parameters are $\{M_\star, m_{20}, \delta, r_{1,\,\mathrm{in}}, r_{1,\,\mathrm{out}}, r_{2,\,\mathrm{in}}, r_{2,\,\mathrm{out}}, m_\mathrm{p}, a_\mathrm{p}\} = \{2\,\mathrm{M}_\odot, 0.2\,\mathrm{M}_\odot, 8\times10^{-3}, 0.03\,\mathrm{au}, 8\,\mathrm{au}, 20\,\mathrm{au}, 200\,\mathrm{au}, 5\,\mathrm{m_J}, 16\,\mathrm{au}\}$. For our parameters, including the stellar torque does not qualitatively change how the inner disc's inclination may be excited by an exterior planet. As the inner disc's precession rate $\dot\Omega_1$ becomes increasingly dominated by the star ($f_{1\star} \gtrsim f_{1\mathrm{p}}$), the secular resonance is crossed earlier (compare right column to left).

3.2.2 *Star + inner disc interactions*

Our modelled inner disc typically has an angular momentum $L_1 = (2/3)m_1\sqrt{GM_\star r_{1,\mathrm{out}}}$ that is less than that of the star S. This fact, together with the inner disc extending down to small stellocentric radii, opens up the possibility that the star controls the precession rate of the inner disc. To the equations modelling the interaction between the inner disc, planet, and outer disc (equations 23–25), we add the contribution from the star to the evolution of the inner disc's orbit normal $\hat{\boldsymbol{l}}_1$:

$$\left.\frac{\mathrm{d}\hat{\boldsymbol{l}}_1}{\mathrm{d}t}\right|_{1\star} = f_{1\star}(\hat{\boldsymbol{l}}_1\cdot\hat{\boldsymbol{s}})\hat{\boldsymbol{l}}_1\times\hat{\boldsymbol{s}}, \tag{47}$$

where the unit stellar spin vector $\hat{\boldsymbol{s}}$ evolves according to:

$$\left.\frac{\mathrm{d}\hat{\boldsymbol{s}}}{\mathrm{d}t}\right|_{\star1} = f_{\star1}(\hat{\boldsymbol{s}}\cdot\hat{\boldsymbol{l}}_1)\hat{\boldsymbol{s}}\times\hat{\boldsymbol{l}}_1 \tag{48}$$

with precession frequencies

$$f_{1\star} = \frac{1}{L_1}\int_{r_{1,\mathrm{in}}}^{r_{1,\mathrm{out}}}\frac{3\pi G M_\star R_\star^2 J_2 \Sigma_1}{r_1^2}\mathrm{d}r_1 \tag{49}$$

$$f_{\star1} = \frac{L_1}{S}f_{1\star}. \tag{50}$$

The effects of the star on the planet (exterior to the inner disc) and outer disc are small and neglected.

Fig. 10 shows the resultant evolution for two values of $P_\star$. We see that inner disc inclinations i_1 become excited by a secular resonance much as they did when stellar spin was ignored (Fig. 5). The star can increase substantially the nodal precession rate of the inner disc

$$\dot\Omega_1 \simeq -f_{1\star}\cos i_1 - f_{1\mathrm{p}}\cos i_1 - f_{12}\cos i_1 \tag{51}$$

but the main consequence is just to cause the secular resonance to be crossed earlier (compare right and left columns of Fig. 10). Our

analytic estimate (36) for i_1 when $\dot{\Omega}_1 = \dot{\Omega}_p$ becomes revised to

$$\cos i_{1,\mathrm{an}} \approx \frac{f_{2p}}{f_{1\star} + f_{1p} - f_{p1} + f_{12}}. \quad (52)$$

Further setting, as we did in Section 2.2, $i_{1,\mathrm{an}}(t) = i_{1,\max}(t_c)$, where t_c is the time when $i_{1,\mathrm{an}}$ first crosses $i_{1,\max}$ (equation 38), predicts to within a factor of 2 the actual i_1.

4 SUMMARY AND DISCUSSION

We have investigated the secular dynamics of two giant planets encircled by a transition disc undergoing mass loss. We have also considered what happens when we replace the inner planet with a disc that is assumed to precess rigidly. We find that:

(i) When the outer planet's angular momentum exceeds the inner planet's, the planets can cross nodal and apsidal secular resonances as the disc disperses. These crossings can magnify the orbital inclination of the inner planet relative to the outer planet and the inner planet's eccentricity. The magnification factor is of order the square root of the ratio of the outer to inner planet's angular momentum (equations 21 and 22). For typical massive two-planet systems, the magnification factor is on the order of a few (Fig. 3). Thus, for example, generating a $\sim 40^\circ$ mutual inclination may require a seed inclination of up to $\sim 10^\circ$ (more on actual systems below). Whether or not a secular resonance is crossed depends in part on the outer disc mass; the crossings simulated in our work rely on outer disc masses initially comparable to the host stellar mass (similar to Class 0/I sources, e.g. Jørgensen et al. 2009; Tobin et al. 2015; Segura-Cox et al. 2018; Andersen et al. 2019).

(ii) Inner discs of the kind observed to reside within the cavities of transitional discs have such low mass (Ubeira Gabellini et al. 2019; Francis & van der Marel 2020; Portilla-Revelo et al. 2023) and, by extension, low angular momentum that their inclinations relative to an exterior planet are more easily amplified by secular resonance. A seed mutual inclination of $\sim 3^\circ$ can grow to $\sim 30^\circ$–90° (Fig. 5). This scenario may explain the tilted inner discs inferred to cast shadows on outer transition discs (e.g. Benisty et al. 2022; Bohn et al. 2022; more on actual such systems below).

(iii) Planet pairs discovered through radial velocity measurements exhibit widely varying degrees of apsidal alignment, from aligned to anti-aligned and everything in between (Fig. 7). The apsidal distribution appears roughly consistent with such pairs predominantly residing on nearly co-planar orbits, with mutual inclinations $\lesssim 20^\circ$. Contrary to Dawson & Chiang (2014), we find no statistical evidence for a separate population of pairs on more highly inclined, apsidally-orthogonal orbits. Such orbits can still exist in principle and might describe individual systems like HD 147018. This system's hypothesized large mutual inclination, but not its large eccentricities, may originate from a secular resonance crossing driven by a decaying outer disc.

(iv) The scenarios we have explored are largely insensitive to the host star's spin, and vice versa. Thus, when the inclination of an inner planet or inner disc is excited, the stellar spin axis does not follow suit; we expect large stellar obliquities.

We close our study by connecting to additional observed systems. Given the angular momentum ratio of a two-planet system, equation (43) estimates the seed inclination i_{20} needed to produce a final mutual inclination i_{mut}. Fig. 11 plots i_{mut} versus i_{20} for systems with measured mutual inclinations. Kepler-448, Kepler-693, and π Men are good candidates for disc-driven, secular excitation of their current inclinations, as they require relatively modest values of $i_{20} \lesssim 10^\circ$ (see also Petrovich et al. 2020). In contrast, because angular momentum ratios are near unity in WASP-148 and ν Andromedae, a secular resonance can do little to magnify the systems' mutual inclinations ($i_{20} \simeq i_{\mathrm{mut}}$). A more promising way to generate their inclinations may be planet–planet scattering (e.g. Chatterjee et al. 2008; Jurić & Tremaine 2008; Barnes et al. 2011; Anderson, Lai & Pu 2020).

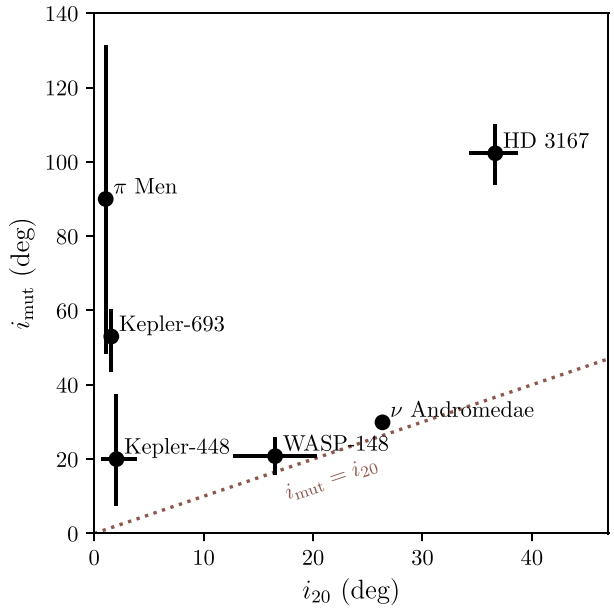

Figure 11. The seed inclination of outer planet i_{20} required to generate the observed mutual inclination i_{mut} (equation 43). The brown dotted line traces $i_{20} = i_{\mathrm{mut}}$. Systems like π Men (Xuan & Wyatt 2020), Kepler-448, and Kepler-693 (Masuda 2017) have large angular momentum ratios L_2/L_1 and can therefore leverage small i_{20} into large i_{mut} using a secular resonance. Other systems like WASP-148 (Almenara et al. 2022) and ν Andromedae (McArthur et al. 2010) have angular momentum ratios closer to unity and are therefore poor candidates for the secular amplification of mutual inclination. See text for discussion of the HD 3167 system (Bourrier et al. 2021) that we hypothesize harbours a distant massive companion. We do not plot KOI-984 (Sun et al. 2022) because the mass and orbital period of the outer companion seem too uncertain; nor do we plot Kepler-108 (Mills & Fabrycky 2017) because its angular momentum ratio $L_2/L_1 < 1$.

The HD 3167 system is particularly puzzling. The planets HD 3167 b and c are transiting sub-Neptunes with orbital periods $P_{\mathrm{orb}} = 0.96$ d and 29.8 d, respectively. The inner member of the pair is nearly coplanar with the host star's equator, and the outer member is inclined by $i_{\mathrm{mut}} \approx 103^\circ$ (Dalal et al. 2019; Bourrier et al. 2021). Although a secular resonance can magnify the mutual inclination between these two planets by a factor of ~ 4 (Fig. 11), HD 3167 c does not have enough angular momentum to also tilt the star (equation 44). A possible solution would be to have a massive distant companion (as yet unobserved) tilt the protoplanetary disc that formed HD 3167 c, leaving HD 3167 b unaffected because of its close proximity to the spinning star (Section 3.2.2). In this scenario, we would also expect the other non-transiting sub-Neptunes in HD 3167 (Bonomo et al. 2023), e ($P_{\mathrm{orb}} = 96.6$ d) and perhaps also d ($P_{\mathrm{orb}} = 8.4$ d), to be approximately co-planar with c.

Other candidates for secular excitation of inclinations include Kepler-56, a system containing two planets of mass 0.07 m_J and 0.56 m_J and periods 10.5 d and 21.4 d, whose orbits are co-planar with each other but inclined relative to the host star's equator by $\sim 45^\circ$ (Huber et al. 2013). A third body detected from radial velocity

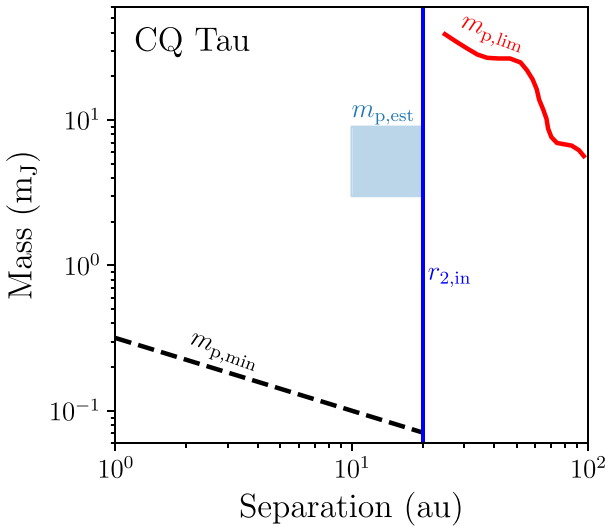

Figure 12. Constraints on the mass of a companion forming within the CQ Tau transition disc. Red solid line plots the companion's maximum mass $m_{\rm p,\,lim}$ at a given location given coronograph non-detections (Uyama et al. 2020; van der Marel et al. 2021). The blue solid line marks the estimated inner cavity edge $r_{2,\,\rm in}$ (Ubeira Gabellini et al. 2019), while the light blue box encloses the estimated mass $m_{\rm p,\,est}$ and semimajor axis of a planet that can carve the disc cavity (Ubeira Gabellini et al. 2019). Black dashed line denotes the minimum companion mass ($m_{\rm p,\,min}$, equation (39)) needed to misalign the inner disc by $i_1 = 44^\circ$ (Bohn et al. 2022), for $m_2 \sim 2.9\,{\rm m_J}$, $r_{2,\,\rm out} \sim 56$ au, and $\delta \sim 10^{-2}$ (Ubeira Gabellini et al. 2019), and $i_{\rm p0} = 3^\circ$ and $r_{1,\,\rm out} = 1$ au assumed arbitrarily. Since $m_{\rm p,\,min} < m_{\rm p,\,est}$, the putative companion can misalign the inner disc and generate CQ Tau's shadows.

observations, with mass $m \sin i = 5.6\,{\rm m_J}$ and period 1000 d (Otor et al. 2016), may have tilted the disc that formed the inner two planets. Another potential application of secular resonance is presented by the warm Jupiter TOI-1859b, hosted by a star with a projected obliquity of $\lambda \approx 39^\circ$ (Dong et al. 2023). An exterior companion larger than a few Jupiter masses (not yet observed), driven by a protoplanetary disc to precess at the right rate, could have misaligned TOI-1895b.

CQ Tau hosts a transition disc with diametrically-opposed shadows (Uyama et al. 2020), thought to be cast by an inner disc inclined by 44° (Bohn et al. 2022). Masses of both the inner and outer discs can be estimated from CO emission, and the mass and location of a planet interior to the disc cavity are constrained from coronagraphic observations and the need to shepherd the cavity edge (Ubeira Gabellini et al. 2019; Uyama et al. 2020; van der Marel et al. 2021). The constraints on the planet are plotted in Fig. 12 (data coloured blue and red), and are completely compatible with a planet that can tilt the inner disc by 44° (black dashed line). The planet mass needed to tilt the inner disc scales linearly with the inner disc mass (equation 39); the latter could be underestimated by nearly two orders of magnitude and still be consistent with our scenario of secular resonance crossing.

ACKNOWLEDGEMENTS

We thank the anonymous referee for their constructive report, which significantly improved the quality of our manuscript. Financial support was provided by NSF AST grant 2205500 and a 51 Pegasi b Heising-Simons Fellowship awarded to JJZ. We thank Rebekah Dawson and Cristobal Petrovich for discussions.

DATA AVAILABILITY

The data underlying this article will be shared on reasonable request to the corresponding author.

REFERENCES

Albrecht S. H., Dawson R. I., Winn J. N., 2022, PASP, 134, 082001
Almenara J. M. et al., 2022, A&A, 663, A134
Andersen B. C. et al., 2019, ApJ, 873, 54
Anderson K. R., Lai D., Pu B., 2020, MNRAS, 491, 1369
Barnes R., Greenberg R., Quinn T. R., McArthur B. E., Benedict G. F., 2011, ApJ, 726, 71
Batygin K., 2018, MNRAS, 475, 5070
Benisty M. et al., 2017, A&A, 597, A42
Benisty M. et al., 2022, ASP Conf. Ser. Vol. 534, Protostars and Planets VII. Astron. Soc. Pac., San Francisco, p. 605
Bi J. et al., 2020, ApJ, 895, L18
Bohn A. J. et al., 2022, A&A, 658, A183
Bonomo A. S. et al., 2023, A&A, 677, A33
Bourrier V. et al., 2021, A&A, 654, A152
Brož M., Chrenko O., Nesvorný D., Dauphas N., 2021, Nat. Astron., 5, 898
Casassus S. et al., 2015, ApJ, 811, 92
Casassus S. et al., 2018, MNRAS, 477, 5104
Chandrasekhar S., 1939, An introduction to the study of stellar structure. University of Chicago Press, Chicago, Illinois, United States
Chatterjee S., Ford E. B., Matsumura S., Rasio F. A., 2008, ApJ, 686, 580
Chiang E. I., Tabachnik S., Tremaine S., 2001, AJ, 122, 1607
Dalal S., Hébrard G., Lecavelier des Étangs A., Petit A. C., Bourrier V., Laskar J., König P. C., Correia A. C. M., 2019, A&A, 631, A28
Dawson R. I., Chiang E., 2014, Science, 346, 212
Debes J. H. et al., 2017, ApJ, 835, 205
Dong J., Foreman-Mackey D., 2023, AJ, 166, 112
Dong J. et al., 2023, ApJ, 951, L29
Eggleton P. P., Kiseleva-Eggleton L., 2001, ApJ, 562, 1012
Epstein-Martin M., Becker J., Batygin K., 2022, ApJ, 931, 42
Francis L., van der Marel N., 2020, ApJ, 892, 111
GRAVITY Collaboration et al., 2021, A&A, 655, A73
Ginski C. et al., 2021, ApJ, 908, L25
Goldreich P., Sari R., 2003, ApJ, 585, 1024
Goldreich P., Tremaine S., 1980, ApJ, 241, 425
Hahn J. M., 2003, ApJ, 595, 531
Heppenheimer T. A., 1980, Icarus, 41, 76
Huber D. et al., 2013, Science, 342, 331
Jørgensen J. K., van Dishoeck E. F., Visser R., Bourke T. L., Wilner D. J., Lommen D., Hogerheijde M. R., Myers P. C., 2009, A&A, 507, 861
Jurić M., Tremaine S., 2008, ApJ, 686, 603
Kluska J. et al., 2020, A&A, 636, A116
Kostov V. B., Moore K., Tamayo D., Jayawardhana R., Rinehart S. A., 2016, ApJ, 832, 183
Kraus S. et al., 2020, Science, 369, 1233
Lai D., 2014, MNRAS, 440, 3532
Lai D., Pu B., 2017, AJ, 153, 42
Lai D., Rasio F. A., Shapiro S. L., 1993, ApJS, 88, 205
Liu B., Muñoz D. J., Lai D., 2015, MNRAS, 447, 747
Long Z. C. et al., 2017, ApJ, 838, 62
Loomis R. A., Öberg K. I., Andrews S. M., MacGregor M. A., 2017, ApJ, 840, 23
Lubow S. H., Martin R. G., 2016, ApJ, 817, 30
Lubow S. H., Ogilvie G. I., 2000, ApJ, 538, 326
Marino S., Perez S., Casassus S., 2015, ApJ, 798, L44
Martin R. G., Lubow S. H., Nixon C., Armitage P. J., 2016, MNRAS, 458, 4345
Masuda K., 2017, AJ, 154, 64
Mayama S. et al., 2018, ApJ, 868, L3
McArthur B. E., Benedict G. F., Barnes R., Martioli E., Korzennik S., Nelan E., Butler R. P., 2010, ApJ, 715, 1203
Mills S. M., Fabrycky D. C., 2017, AJ, 153, 45

Muro-Arena G. A. et al., 2020, A&A, 635, A121
Murray C. D., Dermott S. F., 2000, Solar System Dynamics. Cambridge University Press, Cambridge
Nagasawa M., Ida S., 2000, AJ, 120, 3311
Nagasawa M., Tanaka H., Ida S., 2000, AJ, 119, 1480
Nagasawa M., Ida S., Tanaka H., 2001, Earth Planets Space, 53, 1085
Nagasawa M., Ida S., Tanaka H., 2002, Icarus, 159, 322
Nagasawa M., Lin D. N. C., Ida S., 2003, ApJ, 586, 1374
Nealon R., Dipierro G., Alexander R., Martin R. G., Nixon C., 2018, MNRAS, 481, 20
Nesvorný D., 2018, ARA&A, 56, 137
Otor O. J. et al., 2016, AJ, 152, 165
Owen J. E., Lai D., 2017, MNRAS, 469, 2834
Pérez L. M. et al., 2018, ApJ, 869, L50
Petrovich C., Wu Y., Ali-Dib M., 2019, AJ, 157, 5
Petrovich C., Muñoz D. J., Kratter K. M., Malhotra R., 2020, ApJ, 902, L5
Pinilla P. et al., 2018, ApJ, 868, 85
Portilla-Revelo B. et al., 2023, A&A, 677, A76
Pu B., Lai D., 2018, MNRAS, 478, 197
Rein H., Liu S. F., 2012, A&A, 537, A128
Rein H., Spiegel D. S., 2015, MNRAS, 446, 1424
Segura-Cox D. M. et al., 2018, ApJ, 866, 161
Siegel J. C., Winn J. N., Albrecht S. H., 2023, ApJ, 950, L2
Spalding C., Batygin K., 2017, AJ, 154, 93
Stolker T. et al., 2016, A&A, 595, A113
Stolker T. et al., 2017, ApJ, 849, 143
Sun L. et al., 2022, MNRAS, 512, 4604
Tamayo D., Rein H., Shi P., Hernandez D. M., 2020, MNRAS, 491, 2885
Tanaka H., Ward W. R., 2004, ApJ, 602, 388
Teyssandier J., Lai D., 2019, MNRAS, 490, 4353
Tobin J. J. et al., 2015, ApJ, 805, 125
Ubeira Gabellini M. G. et al., 2019, MNRAS, 486, 4638
Uyama T. et al., 2020, AJ, 159, 118
van der Marel N. et al., 2021, AJ, 161, 33
Vick M., Su Y., Lai D., 2023, ApJ, 943, L13
Ward W. R., 1981, Icarus, 47, 234
Ward W. R., Colombo G., Franklin F. A., 1976, Icarus, 28, 441
Winn J. N., Fabrycky D. C., 2015, ARA&A, 53, 409
Xuan J. W., Wyatt M. C., 2020, MNRAS, 497, 2096
Zanazzi J. J., Lai D., 2017, MNRAS, 464, 3945
Zanazzi J. J., Lai D., 2018a, MNRAS, 477, 5207
Zanazzi J. J., Lai D., 2018b, MNRAS, 478, 835
Zheng X., Lin D. N. C., Kouwenhoven M. B. N., 2017, ApJ, 836, 207
Zhu Z., 2019, MNRAS, 483, 4221
Zhu W., Dong S., 2021, ARA&A, 59, 291

APPENDIX A: SWEEPING SECULAR RESONANCE MODEL

We construct a model for a sweeping secular resonance using Laplace–Lagrange theory. We assume the nodal and apsidal precession periods are much shorter than the disc depletion time $t_{\rm d}$. Equations (3)–(4) and (7)–(8) describe how $\Delta\varpi = \varpi_2 - \varpi_1$ and $\Delta\Omega = \Omega_2 - \Omega_1$ evolve:

$$\frac{{\rm d}\Delta\varpi}{{\rm d}t} = \Delta f - \left(g_{21}\frac{e_1}{e_2} - g_{12}\frac{e_2}{e_1}\right)\cos\Delta\varpi \tag{A1}$$

$$\frac{{\rm d}\Delta\Omega}{{\rm d}t} = -\Delta f + \left(f_{21}\frac{s_1}{s_2} - f_{12}\frac{s_2}{s_1}\right)\cos\Delta\Omega, \tag{A2}$$

where

$$\Delta f = f_{21} + f_{2{\rm d}} - f_{12} - f_{1{\rm d}} \tag{A3}$$

equals the difference between the two planets' non-oscillatory precession frequencies (equations 15–18). For our decaying transition disc scenario, Δf starts positive and decreases with time. Equations (1)–(2) and (5)–(6) imply that eccentricities and inclinations are constant when apses and nodes are either aligned ($\Delta\varpi$, $\Delta\Omega = 0$) or anti-aligned ($\Delta\varpi$, $\Delta\Omega = \pi$). Alignment (+) or anti-alignment (−) is enforced when

$$\left.\frac{e_1}{e_2}\right|_{\pm} = \frac{1}{2}\left[\sqrt{\left(\frac{\Delta f}{g_{21}}\right)^2 + 4\frac{L_2}{L_1}} \pm \frac{\Delta f}{g_{21}}\right] \tag{A4}$$

$$\left.\frac{s_1}{s_2}\right|_{\pm} = \frac{1}{2}\left[\sqrt{\left(\frac{\Delta f}{f_{21}}\right)^2 + 4\frac{L_2}{L_1}} \pm \frac{\Delta f}{f_{21}}\right] \tag{A5}$$

derived by setting (A1)–(A2) to zero. Combining (A4)–(A5) with the conserved quantities (19)–(20) – a.k.a. the angular momentum deficit – yields e_1, e_2, s_1, and s_2 in apsidal/nodal lock. Notice $e_1/e_2|_{\pm}$ and $s_1/s_2|_{\pm}$ have the same value when $\Delta f = 0$:

$$\left.\frac{e_1}{e_2}\right|_{\Delta f=0} = \left.\frac{s_1}{s_2}\right|_{\Delta f=0} = \sqrt{\frac{L_2}{L_1}}. \tag{A6}$$

From hereon, we focus on how inclinations evolve; analogous statements apply for eccentricities. The top panel of Fig. A1 shows $s_1/s_2|_{\pm}$ versus Δf. In the beginning ($t = 0$), $\Delta f > 0$. Which of the aligned or anti-aligned solutions is relevant depends on L_2/L_1 and the initial conditions (including the initial s_{10}/s_{20} and the nodes). As long as Δf changes slowly, the system tends to move along a single + or − track (in reality, oscillating about the track when nodal

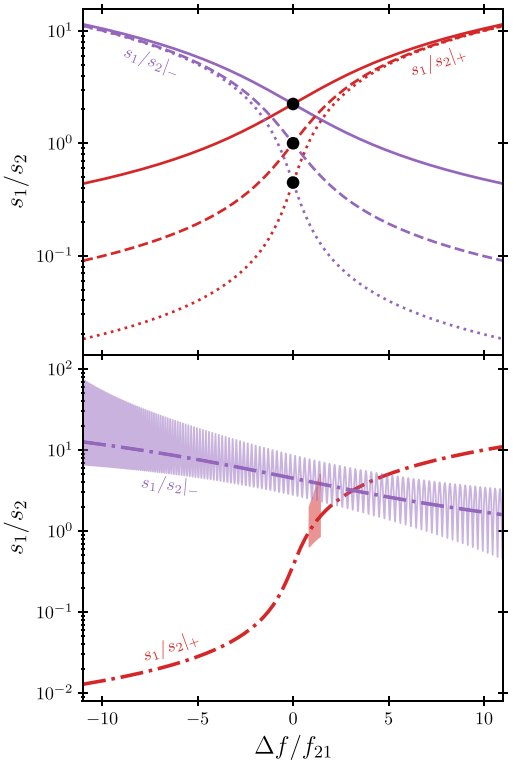

Figure A1. The inclination ratio s_1/s_2 versus $\Delta f/f_{21}$ (equation A5) for the nodally aligned (+, red) and anti-aligned (−, purple) modes. *Top panel*: aligned and anti-aligned solutions for $L_2/L_1 = 5$, 1, and 0.2 (solid, dashed, and dotted lines, respectively). The solutions are symmetric about the critical value $s_1/s_2|_{\Delta f=0} = \sqrt{L_2/L_1}$ (equation A6, solid circles). *Bottom panel*: comparing the full Laplace–Lagrange integrations in Fig. 1 (solid purple, $L_2/L_1 > 1$) and Fig. 4 (solid red, $L_2/L_1 < 1$) to their respective anti-aligned (purple dot–dashed) and aligned (red dot–dashed) tracks. Time advances from right to left. The detuning frequency parameter Δf does not cross zero when $L_2/L_1 < 1$, forestalling large changes to s_1/s_2.

oscillations are non-zero). As Δf decreases, $s_1/s_2|_+$ decreases and $s_1/s_2|_-$ increases, with s_1/s_2 changing most rapidly when Δf crosses zero (secular resonance passage). Because the angular momentum deficit is conserved, the relative $S_k = \frac{1}{2}L_k s_k^2$ values determine how the two orbits exchange inclination. The inner planet's inclination s_1 will amplify most (at the expense of the outer planet's s_2) upon secular resonance passage along an anti-aligned track, for $S_{10} < S_{20}$ initially and $S_{1\mathrm{f}} > S_{2\mathrm{f}}$ in the final state – equivalently, when $s_{10}/s_{20} < \sqrt{L_2/L_1} < s_{1\mathrm{f}}/s_{2\mathrm{f}}$. The various examples given throughout this paper of mutual inclination excitation by secular resonance passage follow this anti-aligned, $L_2/L_1 > 1$ track – a sample evolution taken from Fig. 1 is plotted in the bottom panel of Fig. A1.

In principle, mutual inclination excitation is also possible by following an $L_2/L_1 < 1$, aligned (+) track to decrease s_1 and amplify s_2. But in practice, as explained at the end of Section 2.1.3, Δf never crosses zero when $L_2/L_1 < 1$ in our decaying outer disc scenario, and therefore large changes to s_1/s_2 do not materialize. This is confirmed by the red trajectory, taken from Fig. 4, plotted in the bottom panel of Fig. A1.

This paper has been typeset from a TEX/LATEX file prepared by the author.